STABLE HIGH CONDUCTIVITY BILAYERED ELECTROLYTES FOR LOW TEMPERATURE SOLID OXIDE FUEL CELLS

FETC AAD Document Control Bldg. 921

U.S. Department of Energy

Federal Energy Technology Center

P.O. Box 10940

Pittsburgh, PA 15236-0940

Contract # DE-AC26-99FT40712

Program Manager: Lane Wilson

Semi-Annual Report for Period 10/1/01 - 3/31/02

Eric D. Wachsman and Keith L. Duncan
Department of Materials Science and Engineering
University of Florida
Gainesville, FL 32611-6400

CONTENTS

1. INTRODUCTION

Solid oxide fuel cells (SOFCs) are the future of energy production in America. They offer great promise as a clean and efficient process for directly converting chemical energy to electricity while providing significant environmental benefits (they produce negligible hydrocarbons, CO, or NO_x and, as a result of their high efficiency, produce about one-third less CO_2 per kilowatt hour than internal combustion engines).

Unfortunately, the current SOFC technology, based on a stabilized zirconia electrolyte, must operate in the region of 1000°C to avoid unacceptably high ohmic losses. These high temperatures demand (a) specialized (expensive) materials for the fuel cell interconnects and insulation, (b) time to heat up to the operating temperature and (c) energy input to arrive at the operating temperature. Therefore, if fuel cells could be designed to give a reasonable power output at low to intermediate[1] temperatures tremendous benefits may be accrued. At low temperatures, in particular, it becomes feasible to use ferritic steel for interconnects instead of expensive and brittle ceramic materials such as those based on $LaCrO_3$. In addition, sealing the fuel cell becomes easier and more reliable; rapid start-up is facilitated; thermal stresses (e.g., those caused by thermal expansion mismatches) are reduced; radiative losses ($\sim T^4$) become minimal; electrode sintering becomes negligible and (due to a smaller thermodynamic penalty) the SOFC operating cycle (heating from ambient) would be more efficient. Combined, all these improvements further result in reduced initial and operating costs. The problem is, at lower temperatures the conductivity of the conventional stabilized zirconia electrolyte decreases to the point where it cannot supply electrical current efficiently to an external load.

The primary objectives of the proposed research is to develop a stable high conductivity (> 0.05 S cm^{-1} at ≤ 550 °C) electrolyte for lower temperature SOFCs. This objective is specifically directed toward meeting the lowest (and most difficult) temperature criteria for the 21st Century Fuel Cell Program. Meeting this objective provides a potential for future transportation applications of SOFCs, where their ability to directly use hydrocarbon fuels could permit refueling within the existing transportation infrastructure.

In order to meet this objective we are developing a functionally gradient bilayer electrolyte comprised of a layer of erbia-stabilized bismuth oxide (ESB) on the oxidizing side and a layer of SDC or GDC on the reducing side, see Fig. 1. Bismuth oxide and doped ceria are among the highest ionic

[1] In accordance with current convention, the term "low" is used here to for temperatures < 600 °C while the term "intermediate" refers to temperatures in the range 500-800 °C.

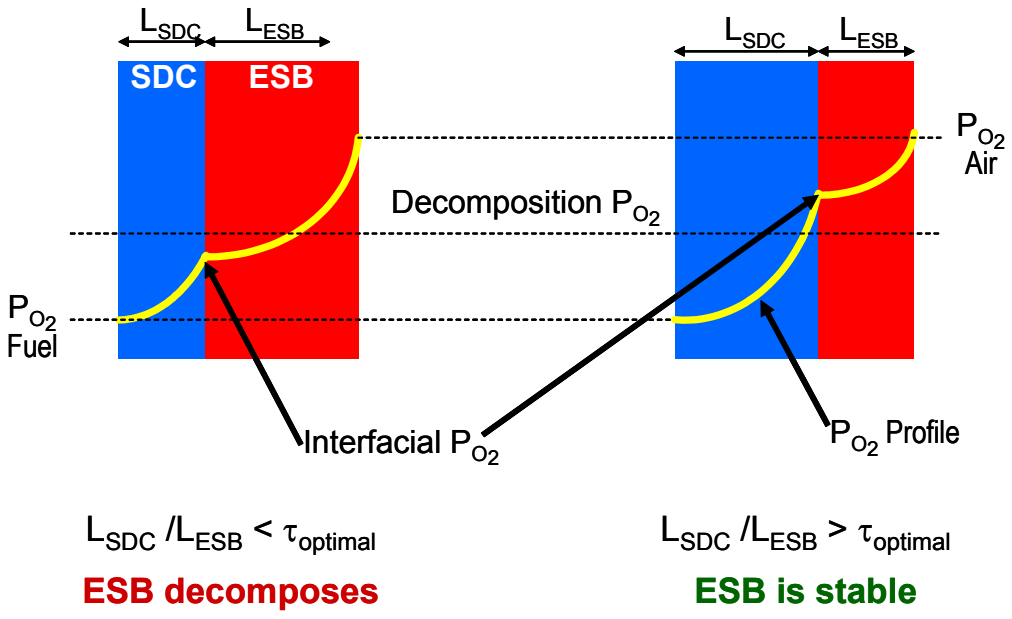

Figure 1. Conceptual representation of a SDC/ESB bilayered electrolyte showing the how the relative thickness can be varied to control the interfacial P_{O_2} to protect the ESB from decomposition.

conducting electrolytes and in fact bismuth oxide based electrolytes are the only known solid oxide electrolytes to have an ionic conductivity that meets the program conductivity goal. In this arrangement, the ceria layer protects the bismuth oxide layer from decomposing by shielding it from very low P_{O_2}'s and the ESB layer serves to block electronic flux through the electrolyte. This arrangement has two significant advantages over the YSZ\SDC bilayers investigated by others [1, 2]. The first advantage is that SDC is conductive enough to serve as an intermediate temperature SOFC electrolyte. Moreover, ESB is conductive enough to serve as a low temperature electrolyte. Consequently, at worst an SDC\ESB bilayered SOFC should have the conductivity of SDC but with improved efficiency due to the electronic flux barrier provided by ESB. The second advantage is that small (dopant) concentrations of SDC in ESB or ESB in SDC, have been found to have conductivities comparable to the host lattice [3, 4]. Therefore, if solid solutioning occurs at the SDC-ESB interface, it should not be detrimental to the performance of the bilayer. In contrast, solid solutions of SDC and YSZ have been found to be significantly less conductive than SDC or YSZ. Thus, it bears emphasizing that, at this time, only SDC\ESB electrolytes have potential in low temperature SOFC applications.

We have previously demonstrated that this concept works, that a bismuth oxide/ceria bilayer electrolyte provides near theoretical open circuit potential (OCP) and is stable for 1400 h of fuel cell operation under both open circuit and maximum power conditions [5]. More recently, we developed an

analytical model to determine the defect transport in this bilayer and have found that a bilayer comprised primarily of the more conductive component (bismuth oxide) is stable for 500°C operation [6, 7].

In this report, the fabrication and characterization of single-layered electrolytes of SDC, ESB and bilayered electrolytes of SDC\ESB are presented as well as the fabrication of anode and cathode materials. Fabrication techniques include standard ceramic processing and the Citrate Process (CP) to produce powders; colloidal deposition and pulsed laser deposition (PLD) to produce thin film layers, screen printing for cathodes application; and uni-axial pressing and cold isostatic pressing (CIP) to produce substrates. Characterization techniques include x-ray diffraction, density analysis, scanning electron microscopy (SEM), x-ray photo-electronic spectroscopy (XPS), energy dispersive spectroscopy (EDS) and electrical impedance spectroscopy (EIS) and current-voltage (I-V) measurements. The report also contains a model for the thermo-mechanical properties of mixed ionic-electronic conductors (MIECs). This model is an extension of the previously reported electrochemical model for the spatial distribution and transport of defects in MIECs.

2. ANODE-SUPPORTED THIN FILM CERIA ELECTROLYTE SOFCs

Investigation of bilayers in the complete range of relative thickness can be accomplished by fabricating anode supported electrolyte by first depositing the ceria layer, the layer with higher sintering temperature and then followed by the Bismuth oxide, the lower sintering temperature layer. Additional benefit of this configuration will come from the fact that anode supported cells show better performance than the cathode supported cells, as in general the anode polarization is lower than the cathode polarization.

We here report the fabrication and initial performance results of an anode supported GDC electrolyte SOFC. Ni-Doped Ceria cermet and $La_{0.6}Sr_{0.4}Co_{0.2}Fe_{0.8}O_3$ was chosen as the anode material and the cathode material, respectively. Doped ceria is a MIEC under reducing conditions at the anode, hence the reaction zone will not be restricted to the interface of the anode and the electrolyte, leading to enhanced performance of the anode. Microstructure plays an important role in the performance of the electrodes, as shown in a recent work by Ohara *et al* [8]. They studied the performance of Ni-Samaria doped Ceria cermet anodes as a function of Ni content and found that at 800 °C, the lowest anodic polarization (~30mV) was achieved for a cermet with a Ni content of around 50vol% at a current density of 300mA/cm^2. Thus, in this work a NiO-Gadolinium doped Ceria (GDC) anode was fabricated with Ni content of 50vol%. Reduction of NiO to Ni was accomplished *in situ*, generating ~26 % porosity in the structure.

Several techniques have been developed for depositing thick films on substrates from vapor deposition techniques (CVD/EVD) and pulse laser deposition (PLD) to chemical routes (sol-gel) among others [9]. However, colloidal deposition has definite advantages over these techniques in its simplicity, cost-effectiveness and flexibility (thickness ranging from 10-100μm can be deposited). Also, exceptional performance has been reported for SOFCs fabricated from colloidal deposition technique by de Souza et al. [10] using a 10μm thick YSZ electrolyte.

Among the cathode materials, $La(Sr)Co(Fe)O_{3-\delta}$(LSCF) and $La(Sr)MnO_{3-\delta}$(LSM) have been extensively studied for fuel cells based on YSZ electrolytes operating at 1000 °C. LSCF is a good electronic conductor (e.g. $La_{0.6}Sr_{0.4}Co_{0.2}Fe_{0.8}O_3$ – 300 S/cm at 750 °C [11]) and also shows fast oxygen surface exchange with high oxygen ion conductivity (e.g. $La_{0.6}Sr_{0.4}Co_{0.2}Fe_{0.8}O_3$ - 10^{-3} S/cm at 750 °C [12]). However, LSCF reacts with YSZ to form resistive zirconate phases at temperatures as low as 800 °C. LSM is stable with YSZ up to temperatures of 1200 °C, but shows lower oxygen ionic conductivity

(10^{-4} S/cm at 900 °C) that limit their application for IT-SOFCs. LSCF does not show any reactions with ceria electrolytes and hence, is the most promising cathode material for IT-SOFCs based on Ceria electrolytes. The Fe rich compositions are attractive as they have lower thermal expansion coefficient and hence, better matched with ceria electrolytes than Co rich compositions [13].

In this report, the fabrication of GDC thick films on NiO-GDC substrates, using a colloidal deposition has been studied. SOFCs were fabricated with $La_{0.6}Sr_{0.4}Co_{0.2}Fe_{0.8}O_3$ as the cathode material and tested in a fuel cell configuration with air/oxygen at the cathode and moist H_2 at the anode under open circuit and closed circuit conditions.

2.1 Fabrication: Colloidal Deposition

11 mol% Gadolinium doped Ceria powder (GDC d_{50} = 0.64 μm) from Rhodia and NiO powder from Alfa-Aesar were mixed and ball milled for 24 hours with Zirconia ball media in Ethanol. The mixed NiO-GDC powder was pressed uniaxially at pressures of 39.3 MPa to form discs of 1.25 inches diameter. The green bodies were then pre-sintered at temperatures between 800 °C to 1100 °C, to coarsen the microstructure and to provide strength for further processing steps.

For the colloidal suspensions, 10 gm of GDC powder was mixed in 100ml of iso-proponal alcohol (IPA). Poly-vinyl Butyral (PVB) in ethanol was added to the solution as binder, equal to 5 - 7 wt% of the oxide powder. The suspension was sonicated in an ultrasonic bath to disperse the GDC powder, with intermittent stirring. The GDC electrolyte layer was deposited on the pre-sintered NiO-GDC discs by dip-coating and finally sintered at 1600 °C and 1650 °C. Multiple coating was done to get thicker films.

The pre-sintering and final sintering temperatures were varied to find the optimum combination at which the densification rate of the GDC film matches with the shrinkage rate of the NiO-GDC anode substrate. This helps in keeping the film under compression rather than in tension and hence, avoiding the cracking of the film due to stress built up by the 2-D confinement during sintering. The diameters of the anode discs were measured after each processing step to calculate the shrinkage profile. Anode samples were reduced in H_2 atmosphere at 800 °C for 5 hours and their density was measured using the Archimedes's principle.

$La_{0.6}Sr_{0.4}Co_{0.2}Fe_{0.8}O_3$ (LSCF d_{50} = 0.7 μm) from Praxiar® was mixed with α-Terpinol, Di-butyl Pthalate, PVB and Ethanol to from the cathode paste. The paste was screen printed on the sintered GDC electrolyte film. The cathode was dried at 100 °C for 1 hr and finally sintered at 750 °C for 1 hr.

2.2 Characterization

The samples were characterized using XRD (APD-3720) and SEM (JEOL-6400) in surface and cross-sectional view. The percentage porosity of the various GDC films was measured by stereological counting methods using point probes.

The representative microstructures of the ceria film with the anode substrates pre-sintered at 800 ºC, 850 °C, 900 °C, 1000 °C, 1100 °C for 4 hours, and after coating finally sintered at 1600 °C for 6 hours and 1650 °C for 10 hours are show in Figs. 2 and 3, respectively. Fig. 4 shows the shrinkage profile of the NiO-GDC anode. Fig. 5 shows the percentage porosity of the GDC film under different sintering profiles. The volume fraction of the porosity in the microstructure is calculated by taking the average fraction of points on a grid, lying on the pores.

The electrode needs to be sufficiently porous to allow for the gaseous diffusion and the electrolyte needs to be highly dense to act as a barrier for the fuel gases and air. The density of the anode substrate after sintering at 1600 °C was measured to be 6.72 gm/cc (~97 % of the theoretical density). On exposure to H_2 atmosphere at 800 °C, NiO in the anode reduced to Ni, which lead to an open porosity of ~20 % and a total porosity of ~29 % in the structure. The anode with an open porosity of ~20 % may be sufficiently porous, but it will be better to increase the porosity of the anode by adding pore-formers. Fig. 6 (a), (b) show the microstructure of the LSCF cathode sintered at 750 °C for 1 hour in the surface and cross-sectional view. Even at this low sintering temperature the cathode looks to have modest porosity, so further work needs to be done to optimize the micro-structure.

As can be seen from Fig. 4, varying the pre-sintering temperature lead to a minima in porosity in the GDC film at 850 °C for both the final sintering temperatures of 1600 °C and 1650 °C, with values of 1.38 % and 1.48 % respectively. However, as can be seen in the Fig. 3, sintering at 1650 °C leads to coarsening of the microstructure. Both the grain and pore size increase and become almost the double the size to that sintered at 1600 °C. Bigger pore size in the electrolyte microstructure has larger chances of failure in partitioning the fuel and air atmospheres in comparison. Also, thermodynamic studies on film stability have shown that, the film thickness should be larger than the grain size of the film for the film to be stable [11]. Otherwise, the film would lower its energy by breaking into isolated islands and exposing the substrate. Hence, it was decided to work with films pre-sintered at 850 °C and finally sintered at 1600 °C for OCP and I-V measurements in a fuel cell configuration.

Density of the GDC film is directly influenced by the stability of the sol, Fig. 7. Increasing the stability of the sol by adding more PVB (7 wt%), leads to an increase in the density of the film at the

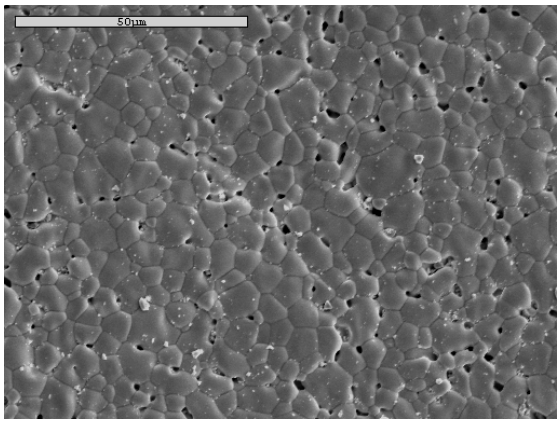

(a)800 °C, 4 hrs/1600 °C, 6 hrs

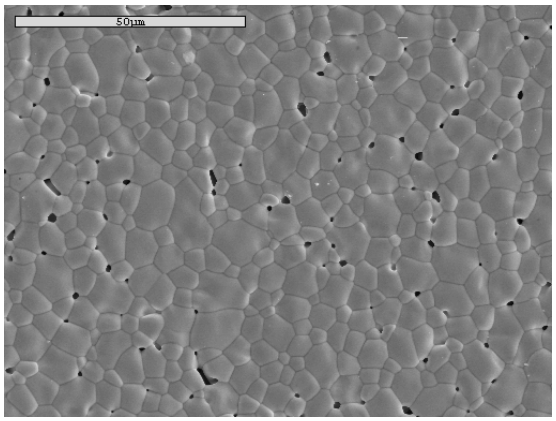

(b)850 °C, 4 hrs/1600 °C, 6 hrs

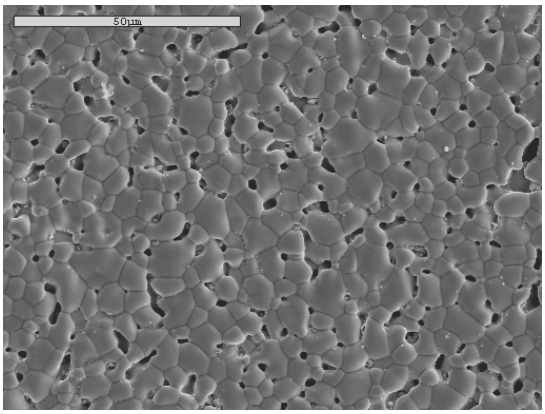

(c) 900 °C, 4 hrs/1600 °C, 6hrs

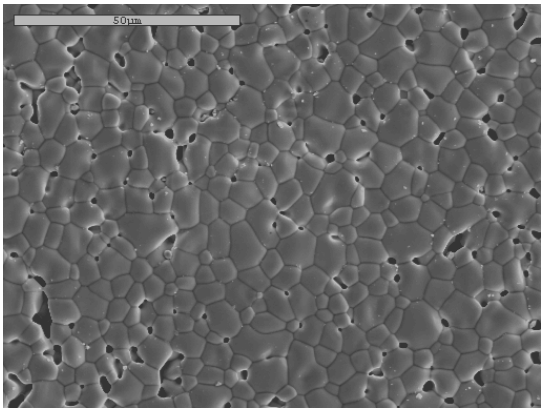

(d)1000 °C, 4 hrs/1600 °C, 6 hrs

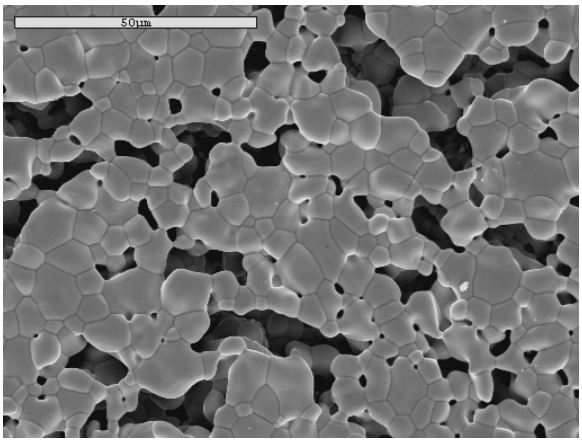

(e) 1100 °C, 4 hrs/1600 °C, 6 hrs

Figure 2. (a)-(e) Representative microstructures of the GDC film under different sintering conditions. (Pre-sintering condition/Final Sintering condition)

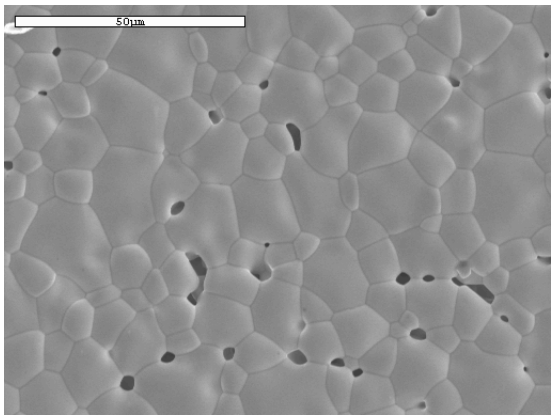

(a) 800 °C, 4 hrs/1650 °C, 10 hrs

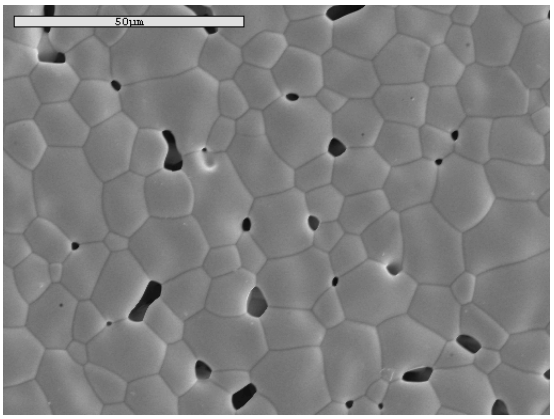

(b) 850 °C, 4 hrs/1650 °C, 10 hrs

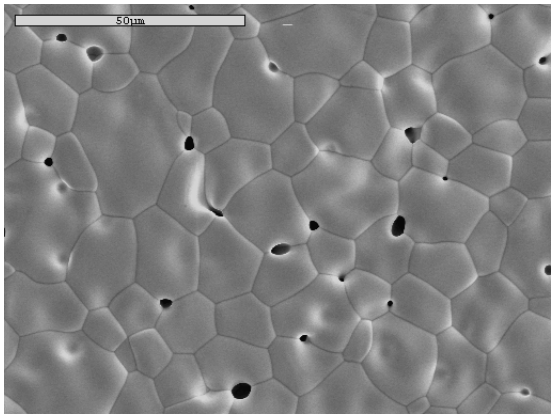

(c) 900 °C, 4 hrs/1650 °C, 10 hrs

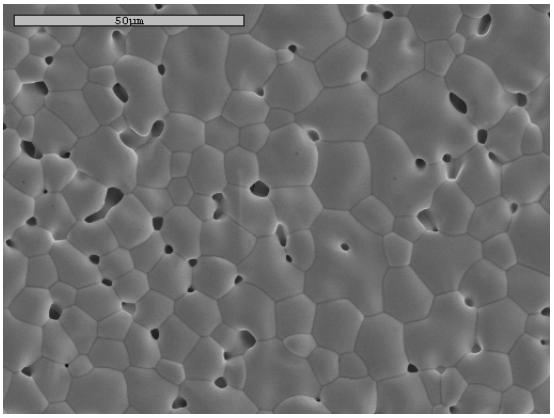

(d) 1000 °C, 4 hrs/1650 °C, 10 hrs

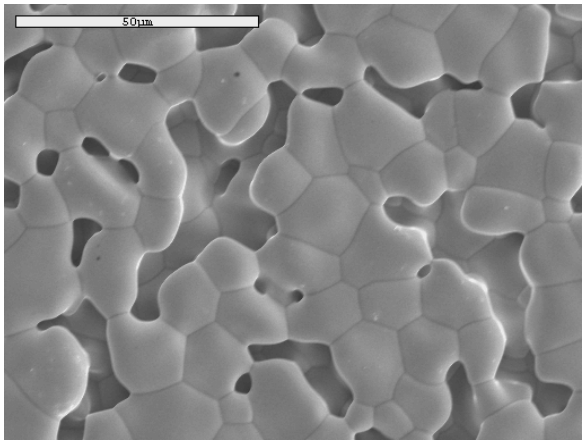

(e) 1100 °C, 4 hrs/1650 °C, 10 hrs

Figure 3. (a)-(e) Representative microstructures of the GDC film under different sintering conditions. (pre-sintering condition/final sintering condition)

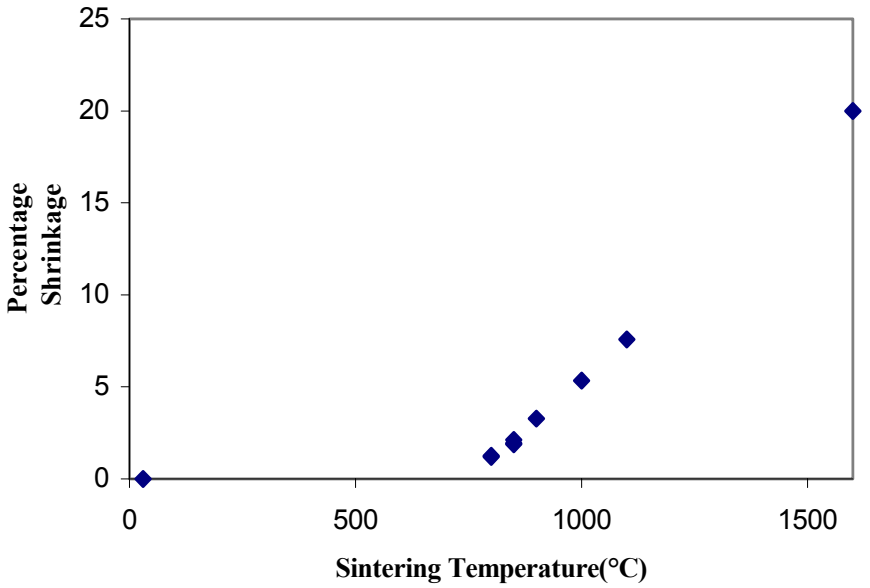

Figure 4. Shrinkage profile of the NiO-GDC anode with sintering temperature.

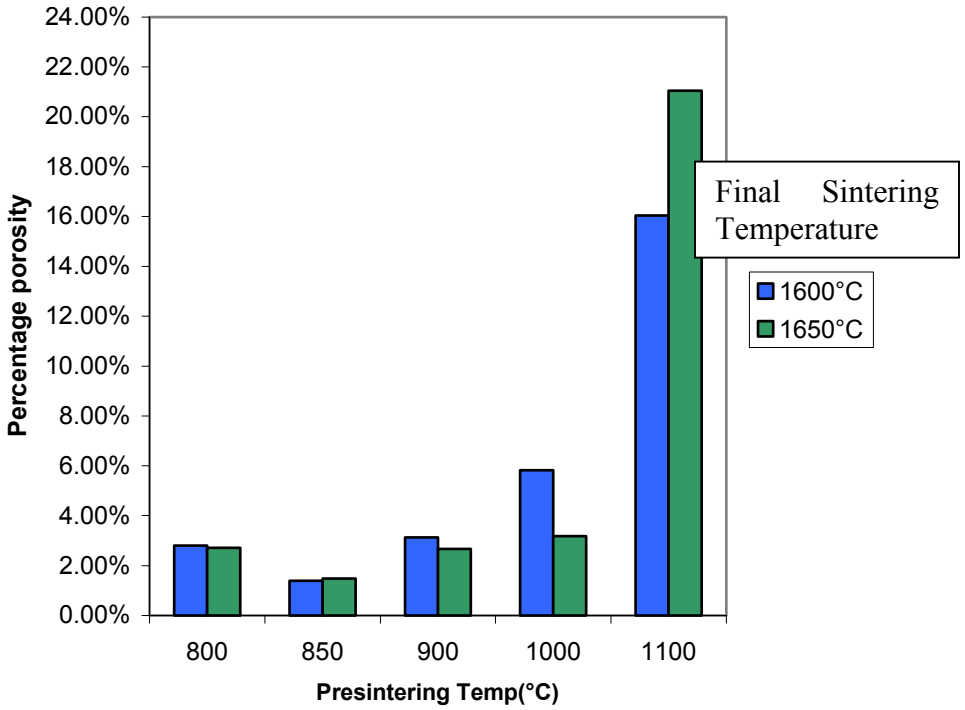

Figure 5. Porosity in the GDC film as a function of the pre-sintering and final sintering temperature of the anode.

(a) 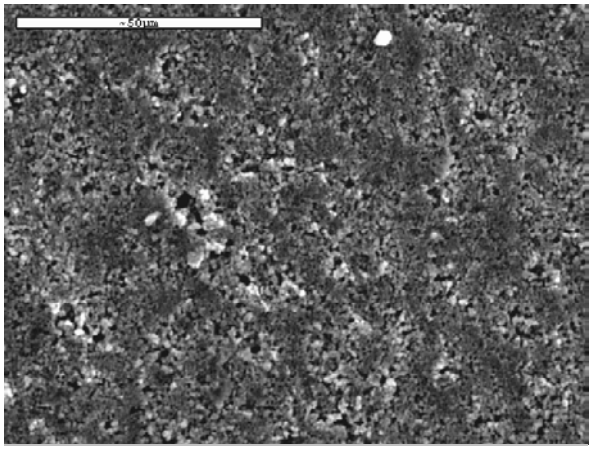 (b) 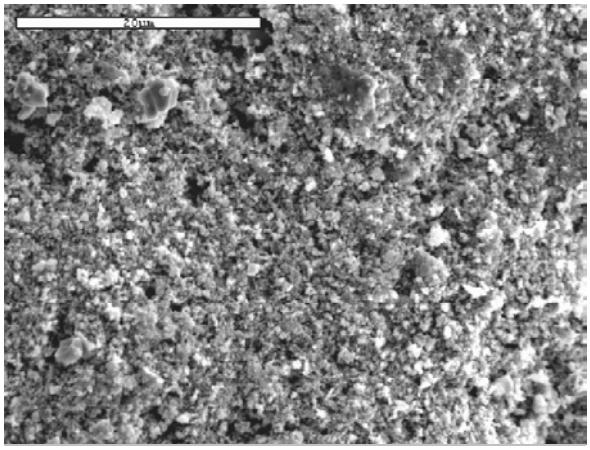

Figure 6. SEM micrographs of the LSCF cathode: (a) Surface (2500X), (b) Cross-section (2000X).

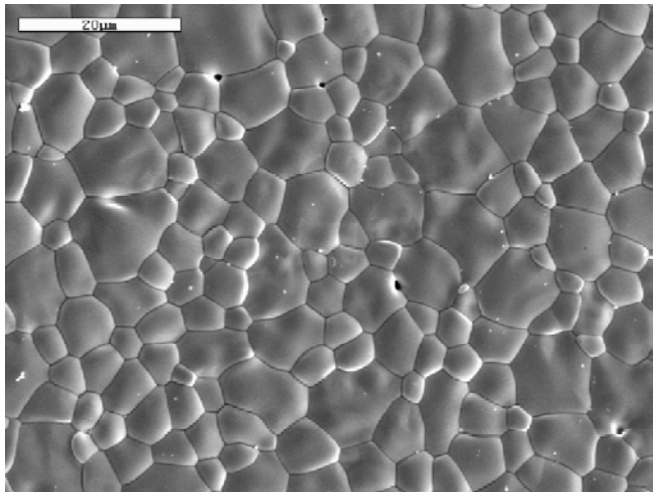

(a) 850 °C, 4 hrs/1600 °C, 6 hrs

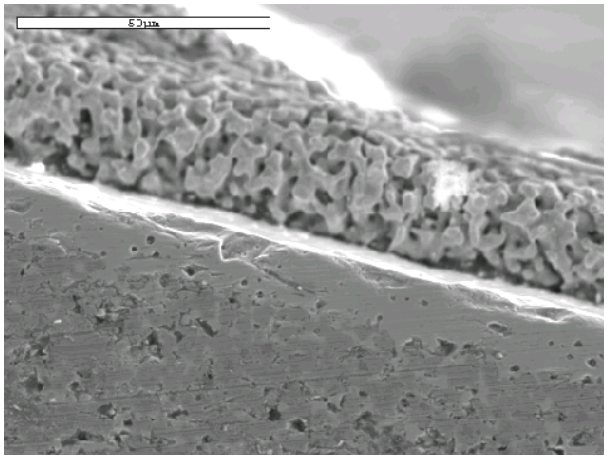

(b) 850 °C, 4 hrs/1600 °C, 6 hrs with 5coats*

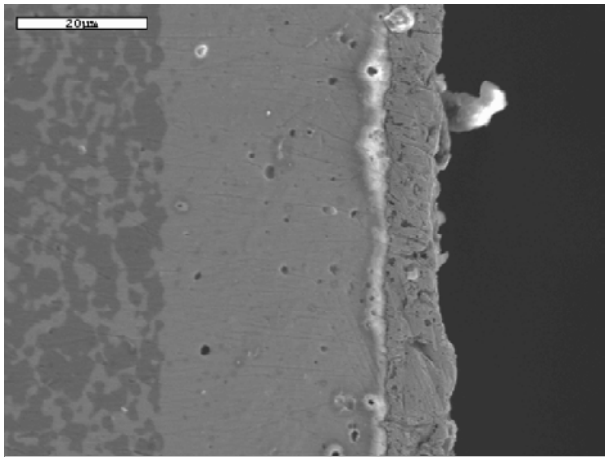

(c) 850 °C, 4 hrs/1600 °C, 6 hrs with 15coats

Figure 7. Increased PVB concentration in the GDC sol (a) Surface microstructure of the film (b),(c) Cross-sectional microstructures of the film with 5 and 15 coats, respectively. (* with reduced anode)

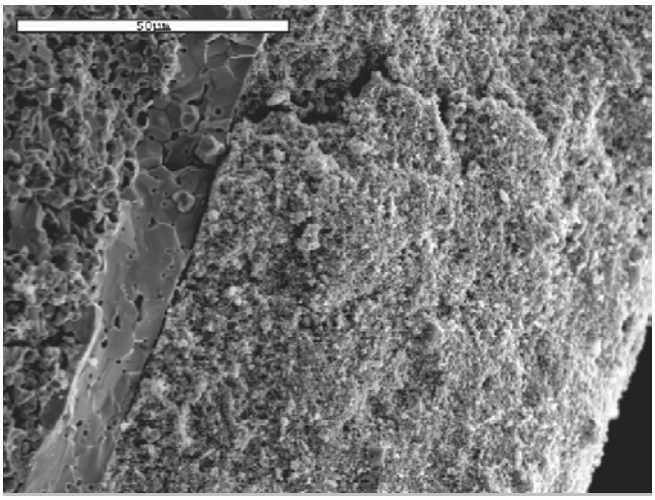

Figure 8. Fractured cross-section of a tested unit cell: Ni-GDC/ GDC (~15μm)/LSCF (~85μm).

same sintering conditions as shown in Fig. 7 (a). Fig. 7 (b), (c) shows the cross-sectional SEM of the GDC film with 5 coats (~10 μm) and 15 (~30 μm) coats, respectively. The film micro-structure shows that it has few closed porosities but no pin holes. Fig. 8 shows the fractured cross-section of a tested unit cell with the reduced Ni-GDC anode, GDC electrolyte (~15 μm) and LSCF cathode (~85 μm).

2.3 Performance

LSCF/GDC/NiO-GDC samples were tested in a fuel cell configuration with air or oxygen at the cathode side and H_2/3%H_2O at the anode side with flow rates of 10-30 sccm at temperatures between 500 °C and 700 °C. The flow rate at the anode and cathode side was kept equal. The Open Circuit Potential (OCP) of the cell was measured using a Keithley multi-meter and the I-V characteristics of the cell were measured using a Solatron Potentiostat/Galvanostat (SI-1287). After an initial transient on exposing the sample to the reducing H_2 atmosphere, due to the reduction of NiO to Ni, the OCP increased and attained a stable value within a few minutes. For the I-V characteristics each data point was collected after 15 minutes to attain a stable value.

The I-V and power density of the cell were measured as a function of temperature, the cathode gas atmosphere and flow rate. Figure 9 is a plot of OCP vs. temperature. At higher temperatures, the electrolytic domain of ceria reduces and the ionic transference number of Ceria decreases. Hence, the OCP of the cell decreases at higher temperatures. As expected, the cell showed a higher OCP with oxygen at the cathode, in comparison to air. Increasing the flow rate lowers the effective P_{O_2} at the anode thereby yielding a higher OCP.

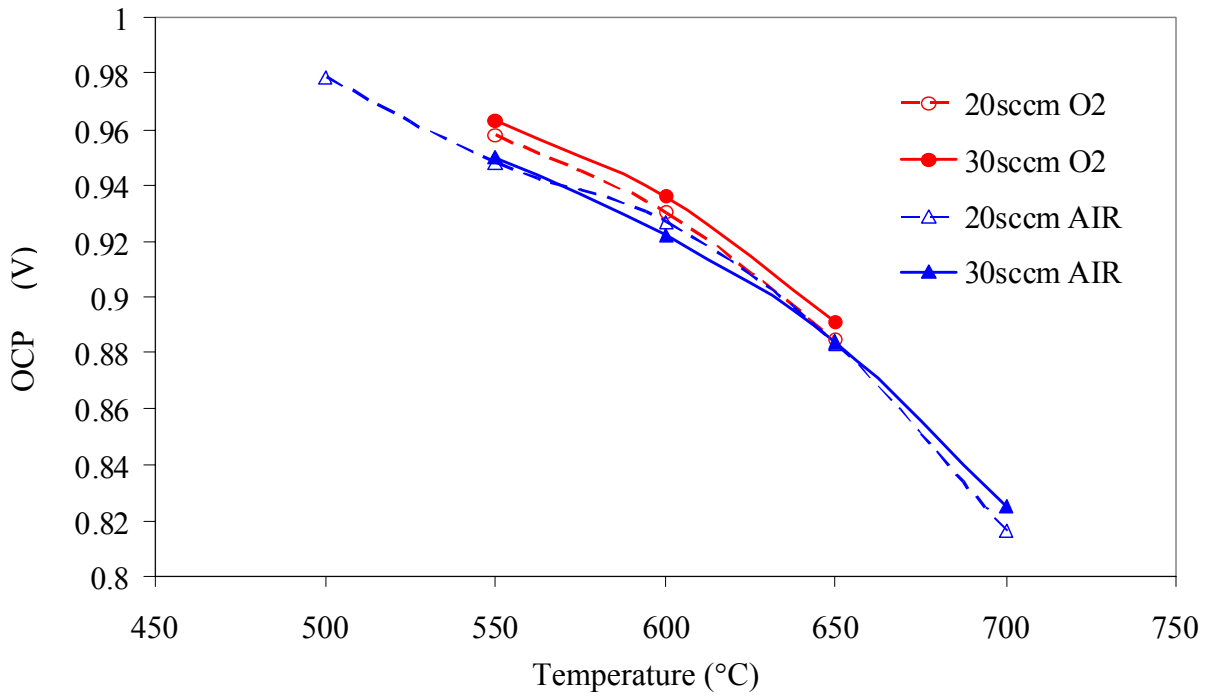

Figure 9. OCP of the cell as a function of temperature, cathode gas atmosphere and the flow rate.

Figure 10 shows the I-V characteristics and power density of the cell with air at the cathode. In open circuit conditions, the cell potential decreased with increasing temperature as shown in Fig. 9. The cell potential also decreased on drawing a current from the cell. The shape of the I-V curves became more linear with increasing temperature. This may be due to lower activation polarization losses at the electrodes at higher temperature. In cells with ceria electrolytes, the power density depends on the conflicting parameters of cell potential and ASR. On increasing the temperature, the cell potential and the ASR both decrease. Hence, there is an optimal temperature where maximum power density is achieved. At 650 °C with a flow rate of 30sccm, the cell showed a power density of 0.25 W/cm^2 at a current density of 0.4 A/cm^2. Even though the ASR of the SOFC at 700 ºC was less, the power density was lower because of the reduced OCP. An ESB layer would raise the OCP resulting in a greater power density at this temperature.

2.4 Conclusion

Ni-CGO anode-supported thin film GDC electrolyte fuel cells were fabricated by a colloidal deposition technique, with an LSCF cathode, and tested in a fuel cell configuration. The density of the film depends on the sintering schedule and the stability of the sol. The cell performance was comparable to those reported in the literature [5, 14]. The cathode performance needs improvement and

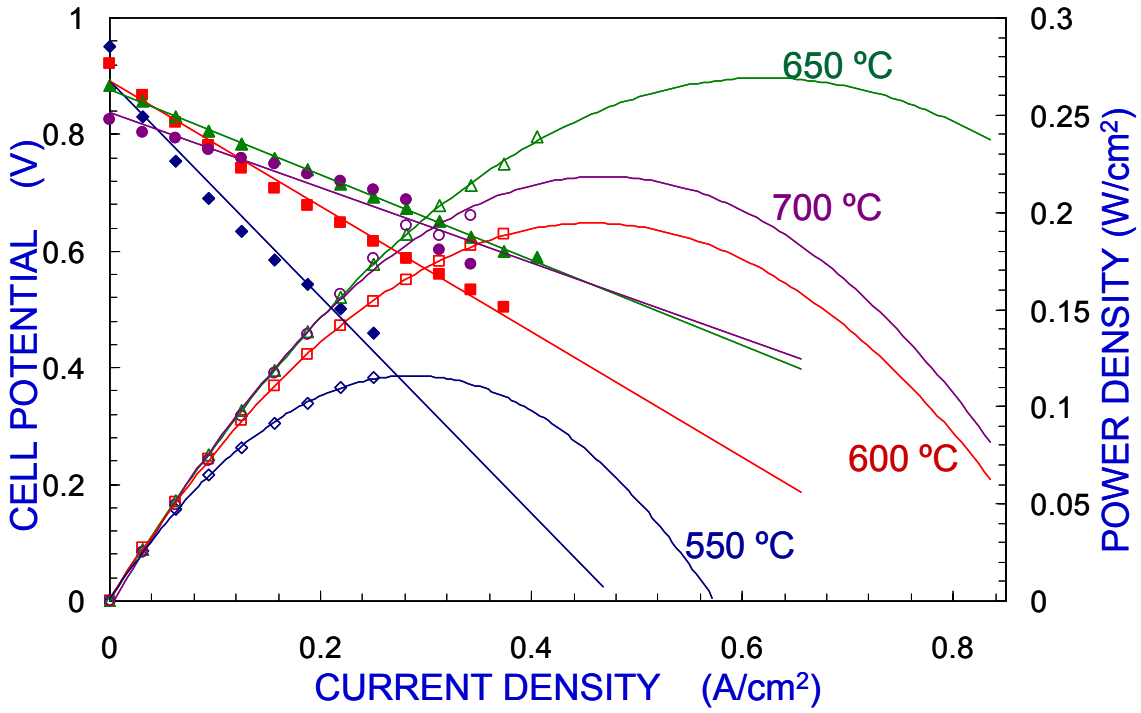

Figure 10. I-V characteristics (closed symbols) and power density (open symbols) of the cell as a function of current density and temperature.

we are developing new cathodes to address this. Further, depositing an electronic blocking layer of ESB on the GDC electrolyte will improve the performance of the cell at intermediate temperatures.

3. BISMUTH OXIDE/CERIA BILAYERED SOFCs

In this section, we describe the synthesis of the precursors for the bismuth oxide/ceria bilayer electrolyte—samarium-doped ceria (SDC: $Ce_{0.8}Sm_{0.2}O_{1.9}$), gadolinium-doped ceria (GDC: $Ce_{0.9}Gd_{0.1}O_{1.95}$), and erbium-stabilized bismuth oxide (ESB: $Bi_{0.8}Er_{0.2}O_{1.9}$)—and cathodes to be used with it. The bilayer electrolyte precursors were synthesized by two processes: solid-state synthesis and the citrate method. Composite cathode materials were prepared exclusively by citrate method.

Fabricating ceria pellets by solid-state techniques required a fairly high temperature of 1600 °C in order to get more than 95 % theoretical density, because of its poor sinterability. Huang et al. [15] demonstrated that the small particle size of the sol-gel prepared materials allows sintering of the samples into highly dense pellets at significantly lower temperature, 1400 °C compared to that of 1600 °C for the samples prepared by conventional method. However, wet-chemical methods are complicated and that limits their application. Despite this, citrate synthesis for multi-component ceramic oxides has gained a reputation for producing very fine, crystalline, and homogenous powders at low decomposition temperature [16, 17]. Accordingly, it offers the advantage of fabricating dense, crack-free, homogenous electrolytes with uniform shrinkage upon heat–treatments at low sintering temperature.

3.1 Solid-State Synthesis Technique (SST)

SDC and GDC electrolytes: Substrate. SDC samples were prepared from polycrystalline powders of ceria and samaria. The powders were weighed to give the appropriate mole fractions and mechanically milled with zirconia media in ethanol for 24 hours. SDC powders were calcined at 1300 °C for 10 hrs, pulverized using a mortar and pestle, and sieved (325 mesh). GDC powder was purchased directly from Rhodia. Both SDC and GDC powders were uniaxially (1450 psi) and isostatically (200 MPa) pressed into disks (diameter < 25 mm and thickness < 2 mm). Finally, the SDC and GDC disks were sintered at 1650 °C and 1550 °C, respectively, for 10 hrs. Theoretical densities were determined by a Philips APD 3720 X-ray diffractometer, and the relative density of sintered bodies was determined by the Archimedes method. The relative densities of SDC and GDC were more than 97 %.

Erbia Stabilized Bismuth Oxide (ESB) Electrolytes: Target. ESB powder was prepared from Bi_2O_3 and Er_2O_3 powders as outlined above for SDC. The powder was calcined at 800 °C for 10 hrs, and uniaxially pressed at 1450 psi. Green bodies were sintered in air at 890 °C for 15 hrs. The resulting

ESB pellets were more than 94 % dense. All specimens were polished with 240 to 1200-grit sandpaper (LECO) to acquire even surfaces and desired thickness.

3.2 Citrate Process (CP)

Electrolytes: SDC, GDC, and ESB. Ceria-based ceramics synthesized by citrate process employed hydrated nitrate salts, $Ce(NO_3)_3{\cdot}6H_20$, $Sm(NO_3)_3{\cdot}6H_20$, and $Gd(NO_3)_3{\cdot}6H_2O$ (99.95 %) from Kanto Chemical. The reactants were dissolved in de-ionized (DI) water then ethylene glycol and citric acid were added as the solvent and the metal chelating agent, respectively. The solution was slowly heated on a hot plate and carefully monitored until the DI water evaporated. At this point, the thermo-chemical reaction between nitrate salts occurred, and a precursor foam was produced. This foam was then fired at 600 °C for 2 hrs to form SDC and GDC powders with fluorite structure. ESB powders were prepared by a similar process using stoichiometric amounts of $Bi(NO_3)_3{\cdot}XH_20$ and $Er(NO_3)_3{\cdot}5H_20$. The post-thermochemical reaction product in this case was a white-yellow ash. The product was calcined at 700 °C for 2 hrs. The crystalline character of the calcined powder was characterized by XRD. For microstructural analysis, the powders were examined using a JSM-35CF scanning electron microscope, which also performed energy dispersive analysis (EDS), a BET (Quantachrome Corporation), and a LS Particle Size Analyzer (Beckman Coulter).

Cathode: $La_{0.85}Sr_{0.15}MnO_3$ (LSM), $La_{0.8}Sr_{0.2}Co_{0.8}Fe_{0.2}O_3$ (LSCF), $Gd_{0.8}Sr_{0.2}MnO$ (GSM), Ag-$Er_{0.2}Bi_{0.8}O_{1.9}$ (Ag-ESB). All powders (except Ag) were prepared using the citrate method described above and calcined at 700 °C for 4hrs. The starting materials for synthesis are shown in Table 1. All powders (except Ag-ESB) were milled for 24 hrs in ethanol, using zirconia media, to form cathode inks.

Table 1. Starting materials used for the synthesis of LSM, GSM, GLSM (GDC+LSM), GGSM (GDC+GSM), LSCF, ESB, SDC, and GDC powers by citrate process (CP)

Starting materials	Purity (%)	Makers
$Ce(NO_3)_3{\cdot}6H_20$	99.99	Kanto Chemical
$Sm(NO_3)_3{\cdot}6H_20$	99.95	Kanto Chemical
$Gd(NO_3)_3{\cdot}6H_20$	99.95	Kanto Chemical
$Er(NO_3)_3{\cdot}5H_20$	99.99	Alfa Aesar
$Bi(NO_3)_3{\cdot}XH_20$	99.999	Alfa Aesar
$La(NO_3)_3{\cdot}6H_20$	99.99	Adrich
$Sr(NO_3)_2$	99.5	Kanto Chemical
$Mn(NO_3)_3{\cdot}XH_20$	99.99	Alfa Aesar
$Co(NO_3)_2{\cdot}6H_20$	98.5	Alfa Aesar
$Fe(NO_3)_3{\cdot}XH_20$	99.999	Alfa Aesar

Table 2. Screen print slurry formation for cathode materials

Materials	Function	Amount per gram of powder
α-terpineol	Solvent	0.5cc
Dibutyl phtalate	Plastcizer	0.05cc
Polyvinyl butyral	Binder	3 wt.%

The slurries were mixed in a mortar and pestle until an appropriate viscosity was reached then screen-printed onto the bilayer ESB/GDC and ESB/SDC electrolytes, and fired at 900 °C for 1 hour. Ag-ESB cathodes were sintered at 800 °C for 1 hour due to the low melting temperature of silver. After sintering of cathode materials, Ag wires were attached to the electrodes using Ag paint, dried and sintered at 800 ºC to ensure good contact between cathodes and current collectors.

3.3 Thin Film Preparation

Oxide thin films have been prepared by a variety of methods such as spray RF ion plating [18], laser spraying [19], spray pyrolysis [20], sputtering [21], chemical vapor deposition (CVD) [22], and pulsed laser deposition (PLD) [23]. PLD is suitable for preparing high-quality thin films of multi-component oxides. This technique requires temperature around 500 °C to 700 °C. The bilayer electrolytes can also be produced by slurry coating [24, 25]. One of the advantages of slurry coating over PLD is that up-scaling to component size and volume is much more practical. Dip-coating is one example of a slurry coating technique. This procedure is simple, has precise composition control, and is a low processing temperature technique. This study used both PLD and dip-coating techniques to fabricate of ESB thin films on either SDC or GDC substrates.

3.3.1 Pulsed-Laser Deposition: PLD

Figure 11 shows a typical PLD system. ESB thin films were deposited on one side of polished SDC substrates. Film thicknesses were measured by profilometry (Alpha-step 500, Tencor) around the outer edge of the samples where two small sample holders were placed to mask these areas from deposition. The frequency of the KrF excimer laser (Lambda Physik) was set at 10Hz, and the laser energy was 500 mJ, yielding a substrate temperature of 700 °C.

3.3.2 Colloidal Deposition: Dip-Coating

Bilayers were also fabricated via dip-coating. For this process, 5 wt.%, 7 wt.%, and 10 wt.% ESB slurries were prepared and dip-coated on one side of the substrate. The dipping cycle was repeated to obtain the desired thickness of the electrolyte. The film-coated bilayer electrolytes were then sintered at

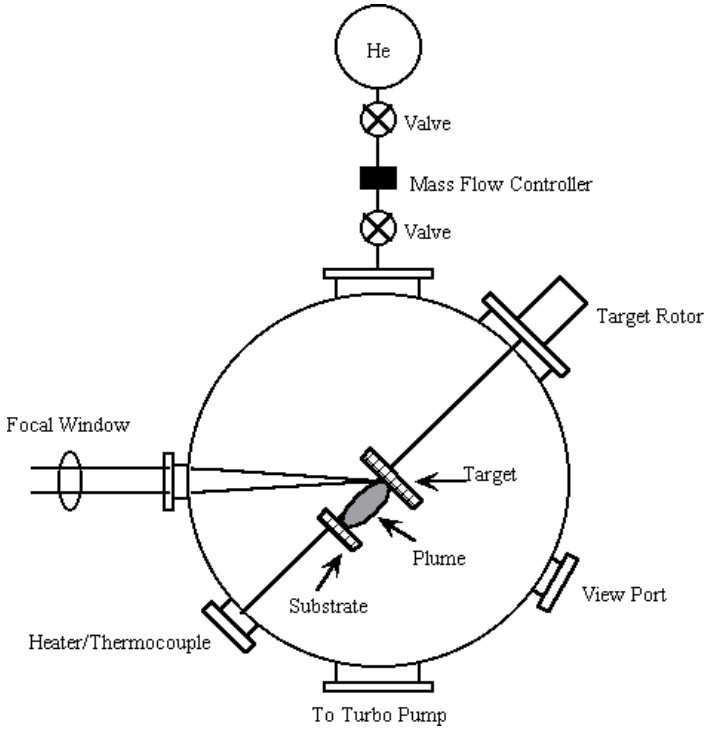

Figure 11. Experimental system of pulsed laser deposition (PLD) [26].

890 °C for 10 hrs. XRD, SEM, and EDS were performed to analyze quality of the film and to measure the film thickness. A more detailed description of this technique is provided in chapter 2.

3.4 Characterization

3.4.1 Characterization of ESB, GDC, and SDC Powders

Figure 12 shows that the structure development of the ESB precursors by XRD. As the calcining temperature increases, the fluorite structure is identified more clearly, and finally formed at 700 °C. There are no second phase, such as nitrates and carbonates, present. Figure 13 shows representative XRD patterns of powders synthesized by both conventional solid-state technique (SST) and citrate process (CP). Conventionally synthesized powders by SST are identical to those of powders by CP, and confirm the formation of cubic SDC, GDC, and ESB. SEM micrographs in Fig. 14 show the powders synthesized by CP have more faceted polyhedral morphologies, whereas particles by SSP exhibited elliptical morphologies. The average particle size, measured by TEM micrographs and particle size analyzer, of powders synthesized by CP and by SST was 20 – 40 nm and 100 – 250 nm, respectively. The powders prepared by CP were less dense and had higher surface area than those fabricated by SST, as shown in Table 3. There was no significant difference in the surface area and SEM morphology of the GDC powders synthesized by CP and from Rhodia®. Since particle shape and size distribution, and

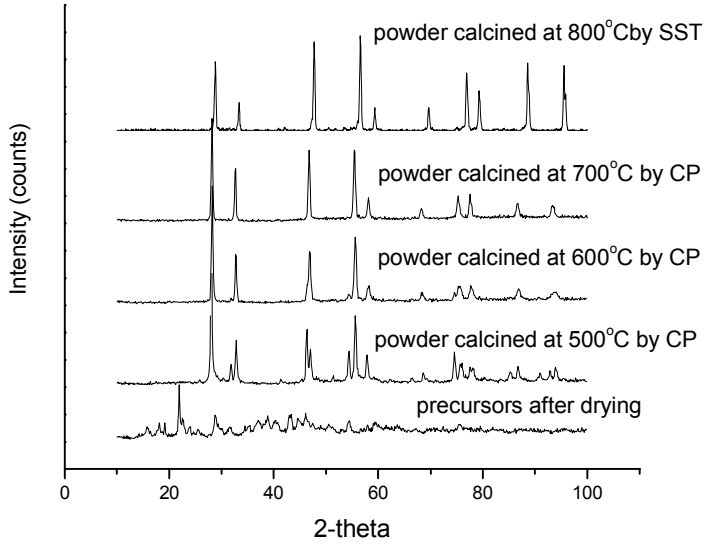

Figure 12. Structural development to fluorite structure by X-ray diffraction patterns of ESB precursors as increasing calcining temperature

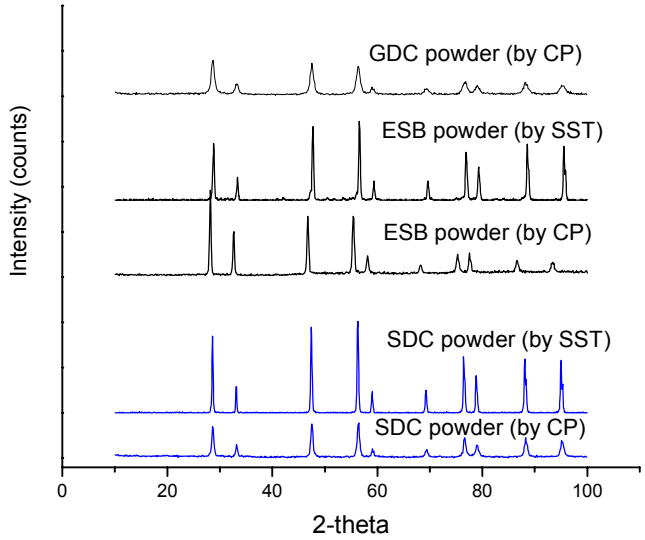

Figure 13. XRD patterns of calcined SDC, GDC, and ESB powder fabricated by SST and CP

Table 3. Specific surface area and pore volume and diameter of cathode precursors

Materials	**BET (m^2/g)**			**Pore Volume (cc/g)**	**Pore Diameter (Å)**	
	Multipoint BET	Langmuir method	BJH method	Total pore volume	Average pore dia.	BJH method
GDC (CP)	38.8	70.3	51.7	0.269	277.7	38.4
GDC (Rhodia)	24.9	45.0	30.9	0.328	524.5	19.1
SDC (CP)	53.5	88.1	81.7	0.276	206.3	18.8
SDC (SST)	36.8	65.5	45.2	0.546	593.1	18.9
LSM (CP)	19.0	33.0	19.1	0.258	543.3	18.9
GDC+LSM	37.5	65.4	37.9	0.187	199.3	38.2
GSM (CP)	47.8	84.3	52.1	0.324	270.6	95.8

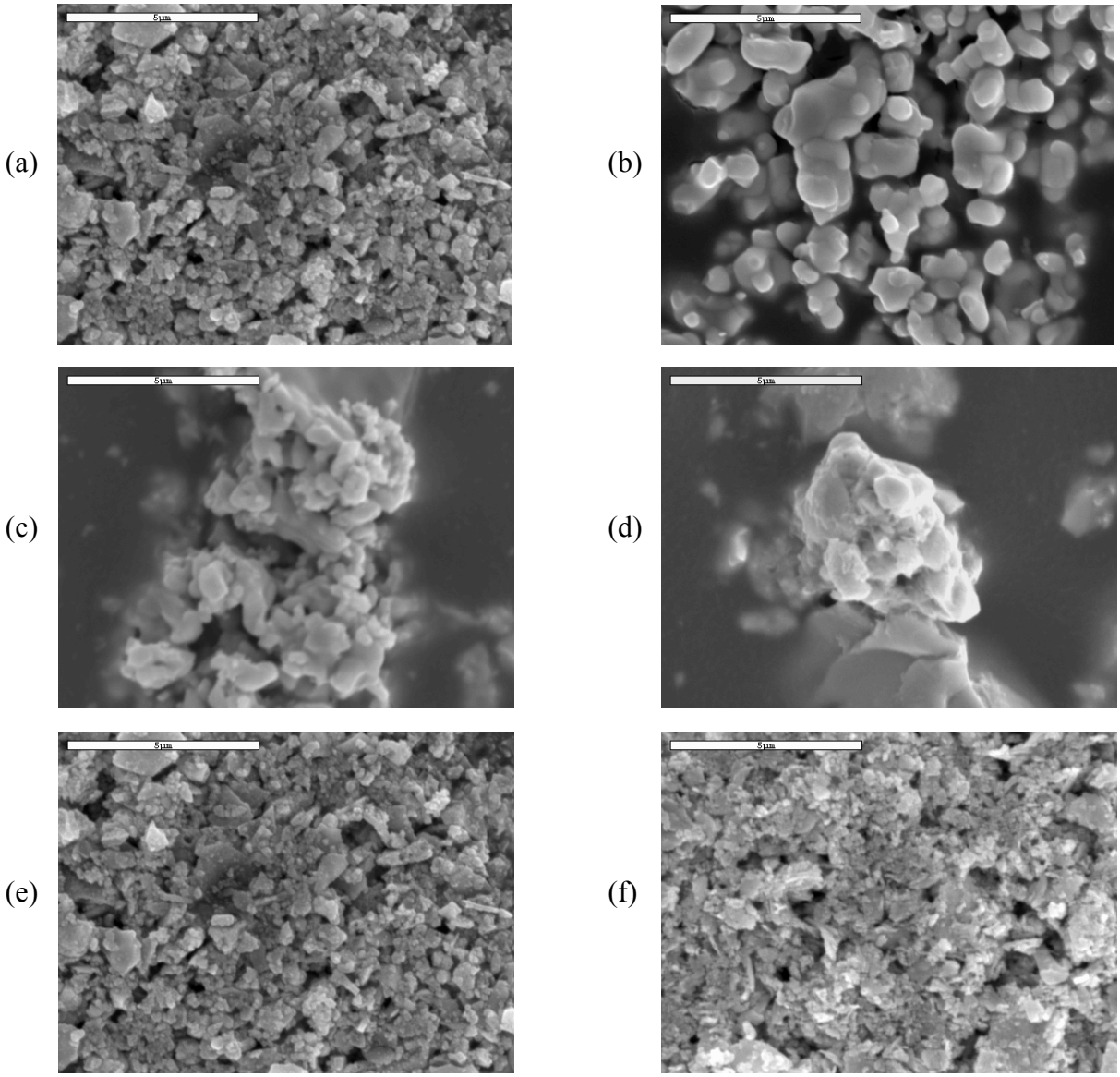

Figure 14. SEM micrographs of SDC powder (a) by CP (b) SST, ESB powder (c) by CP, (d) by SST, and GDC powder (e) by CP (f) from Rhodia®.

high surface area influence the packing and the flowability of the powder in the filling of dies during compaction, the ESB, GDC, and SDC powders synthesized by CP could acquire high-density bulk samples at lower sintering temperatures.

3.4.2 Characterization of Powders for the Cathode

The XRD patterns of the LSM and LSCF powders in Fig. 15 show they have a perovskite single phase structure. Figure 15 further shows that the composites GDC+LSM (GLSM) and GDC+GSM (GGSM) have both fluorite and perovskite structures present. Figure 16 shows SEM images of LSM, GSM, and composite GLSM cathodes. The particle size and porosity of LSM particles appear smaller

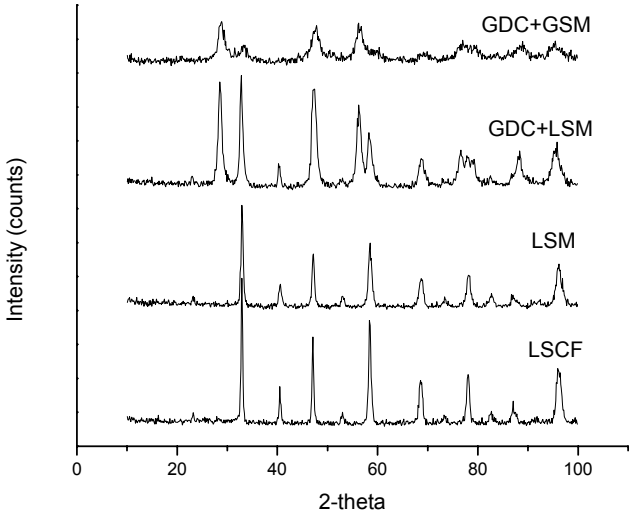

Figure 15. XRD patterns of calcined LSM, GLSM, GGSM, and LSCF powders by fabricated CP

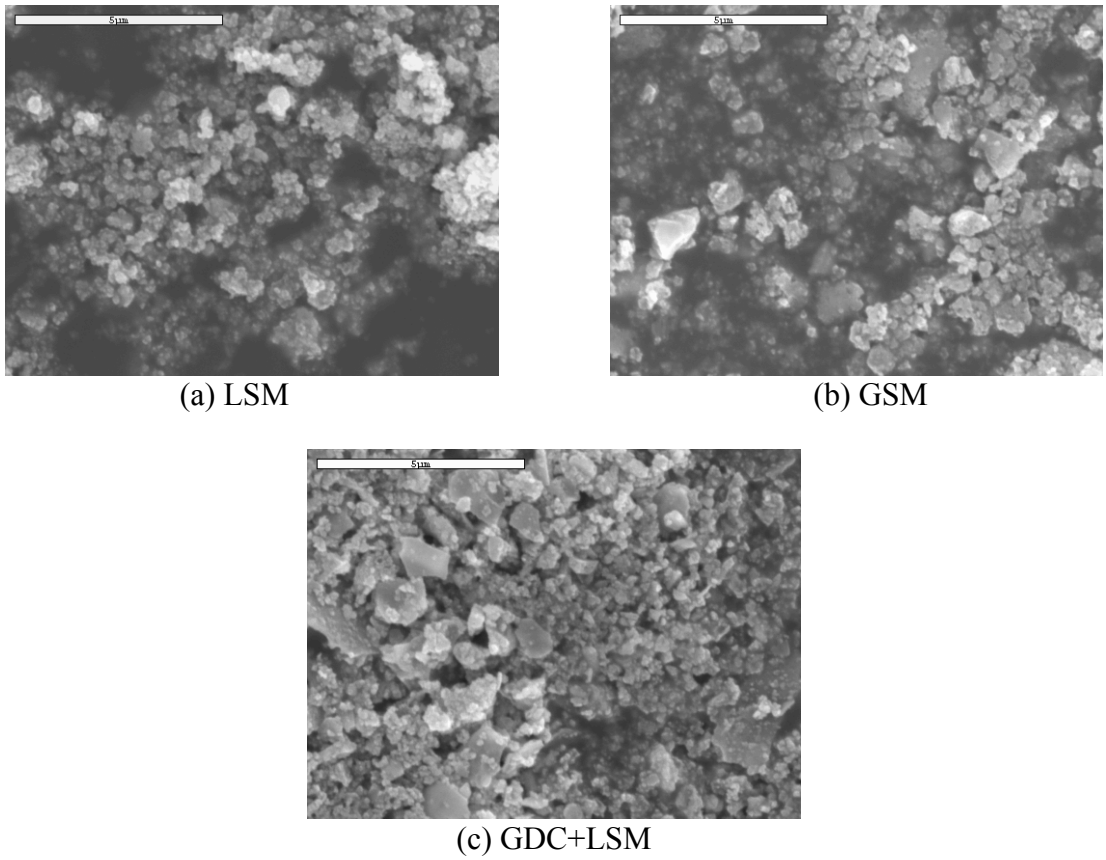

(a) LSM (b) GSM

(c) GDC+LSM

Figure 16. SEM micrograph of LSM, GSM, GDC+LSM cathode materials

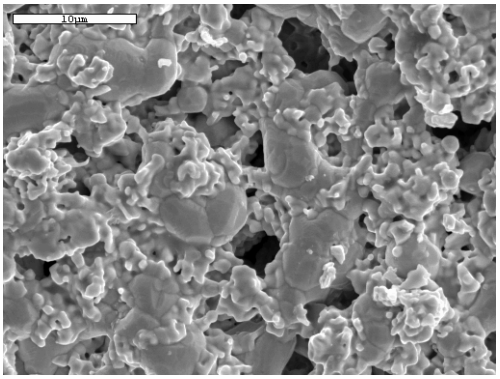

(a) surface images of Ag-ESB

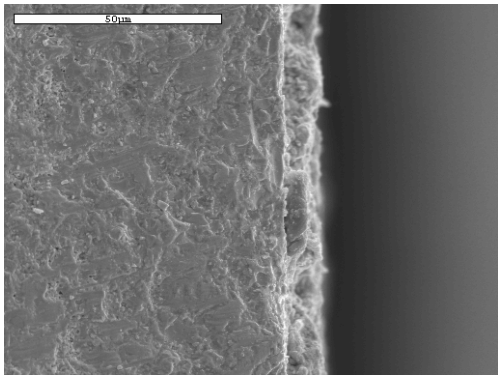

(b) cross-section of Ag-ESB on ESB substrate

Figure 17. SEM images of Ag-ESB composite cathode.

than that of the GDC and GLSM, but the shapes of the particles are more spherical in the GSM and GLSM. This observation provides further support for the idea that the irregularly shaped particles in the GSM and GLSM cathodes were GDC.

A range of two-phase Ag-ESB cathodes were also investigated. The cathodes were applied in the form of screen printing inks to the electrolyte and sintered at 800 °C as described earlier. Figure 17 shows typical surface and cross-sectional images of an Ag-ESB cathode, with the ESB electrolyte. The Ag and ESB particles appear to have sintered well with each other and bonded well at the Ag-ESB/ESB interface. The ESB cathode differs in that the particles have rounded edges and are smaller in size compared to those of Ag powder. There was a ~3 μm interaction layer between the electrolyte and the ESB in the cathode. The polarization resistance for the porous Ag-ESB cathodes as a function of vol.% Ag was evaluated by Doshi *et al* [27] and found to exhibit a minimum between 45 and 55 vol.%.

3.4.3 Characterization of Bilayer ESB/SDC and ESB/GDC Electrolytes

Pulse Laser Deposition (PLD). The XRD patterns of bilayer ESB/SDC electrolytes by PLD are also equal to that of cubic ceria and bismuth oxide as shown in Fig. 18. This result indicates that there are insignificant amounts of other phases resulting from the interfacial reactions between SDC and ESB and, therefore, by extension, PLD is an adequate means to deposit ESB on an SDC substrate.

Figure 19 is a cross-section SEM micrograph of the ESB film on a dense SDC substrate, via PLD, showing that the film adheres well to the SDC substrate. The chemical composition of the bilayered ESB/SDC electrolytes was estimated from energy dispersive analysis (EDS), Fig. 20. Significant solid-state reaction or interdiffusion between the phases was not detected from their EDS or XRD patterns.

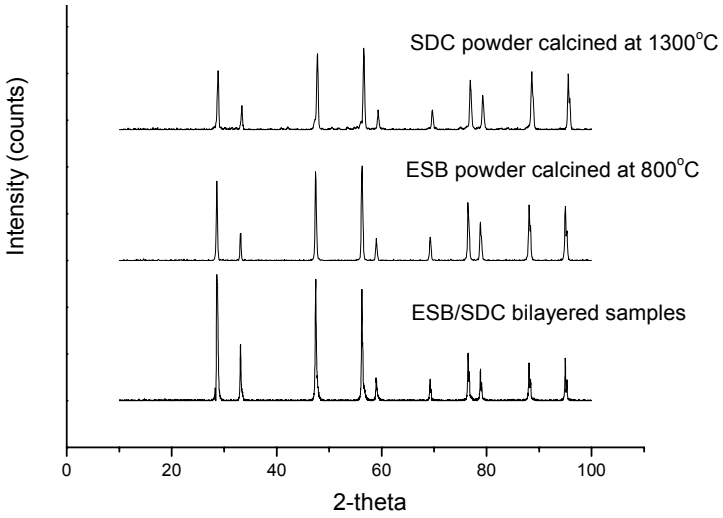

Figure 18. X-ray diffraction patterns of calcined SDC powder at 1300 °C for 10hrs, calcined ESB powder at 800 °C for 16hrs, and SDC coated with ESB (ESB film thickness: 0.2 μm) via PLD.

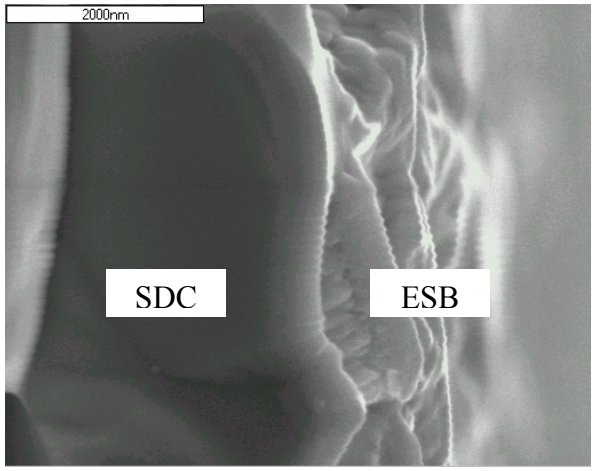

Figure 19. Cross-section SEM micrograph of the ESB film on dense SDC substrate via PLD

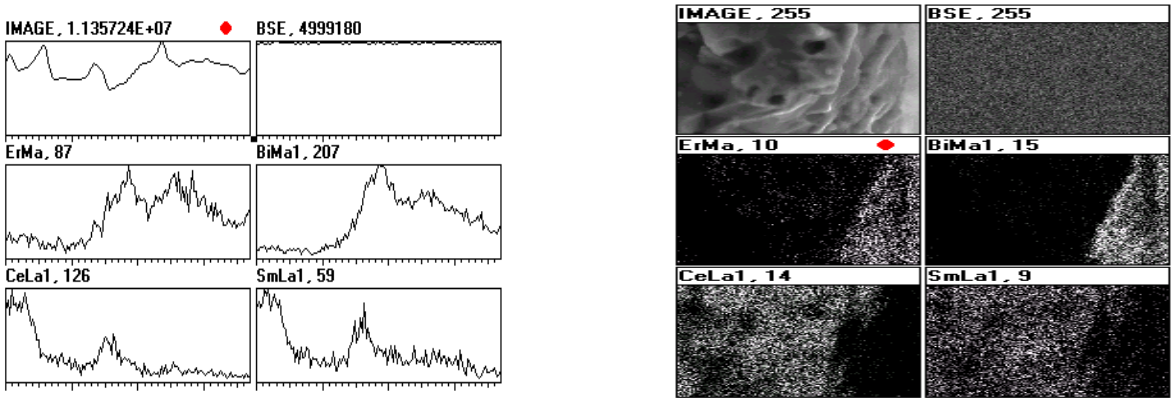

(a) X-ray linescan of elements (b) X-ray map of elements

Figure 20. The chemical composition of the bilayer ESB/SDC electrolytes estimated from EDS by X-ray linescan and mapping.

Dip-coating. The Dip-coating method was also used to apply an ESB film to form ESB/SDC bilayers. Three different concentrations of the ESB gel were used, resulting in a final film thickness ranging from 9 to 30 μm, by SEM micrograph. Figure 21 is the cross-section SEM micrograph of the different ESB film on dense SDC substrate via dip-coating. It shows that the film adheres well to the baseline SDC substrate. However, both film thickness and densification of ESB film increased with the amount of ESB in the sol. The film fabricated by 5 wt.% ESB gel exhibited porous film surface, but with the 10 wt.% ESB gel a dense film surface was obtained. Concentrations of more than 10 wt.% ESB did not form a stable gel for coating. The process needs further work to improve the stability of the gel

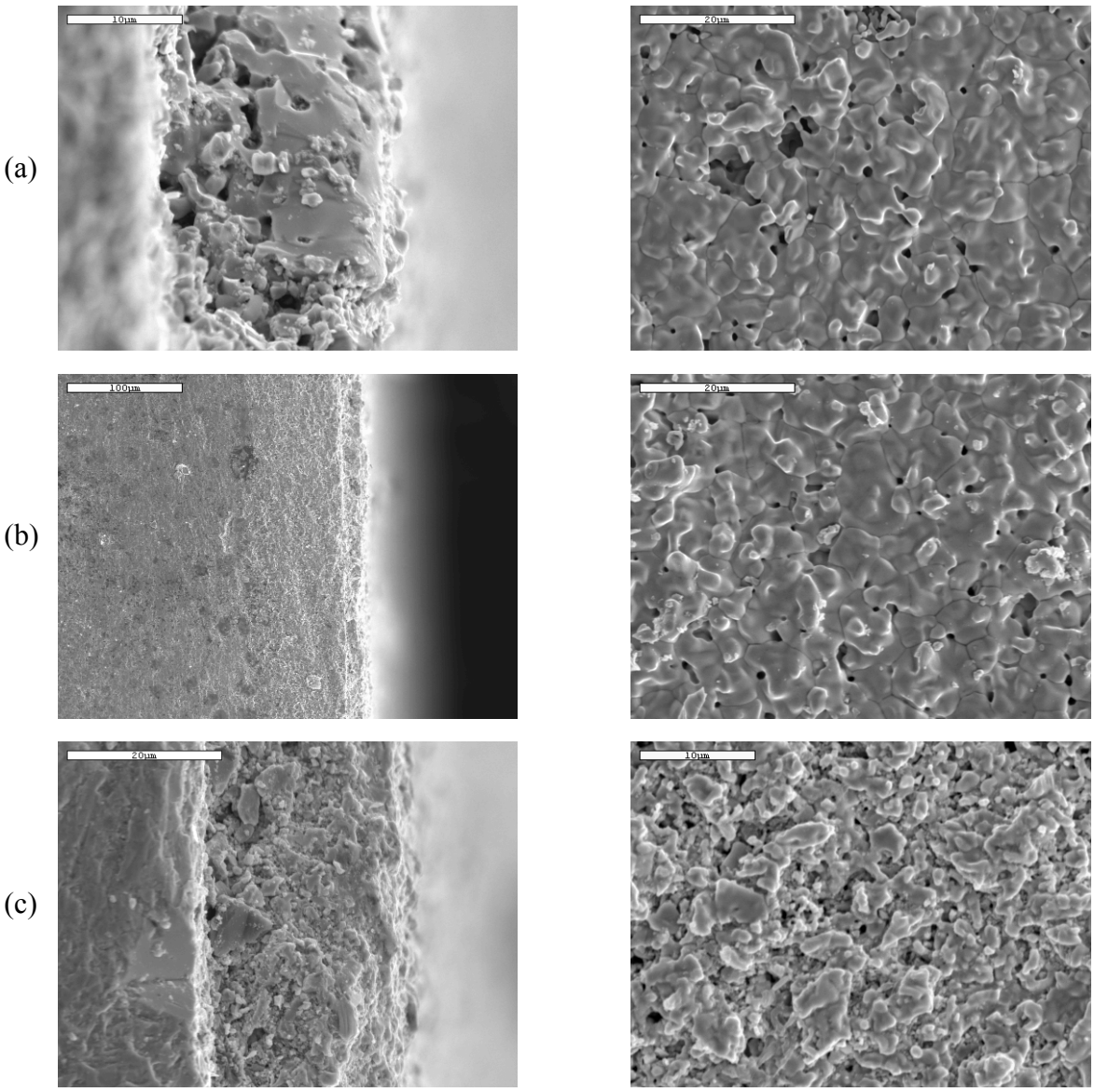

Figure 21. Cross-section SEM micrograph of the ESB film on dense SDC substrate via dip-coating: (a) 5wt.%, (b) 7wt.%, and (c) 10wt.% ESB solution

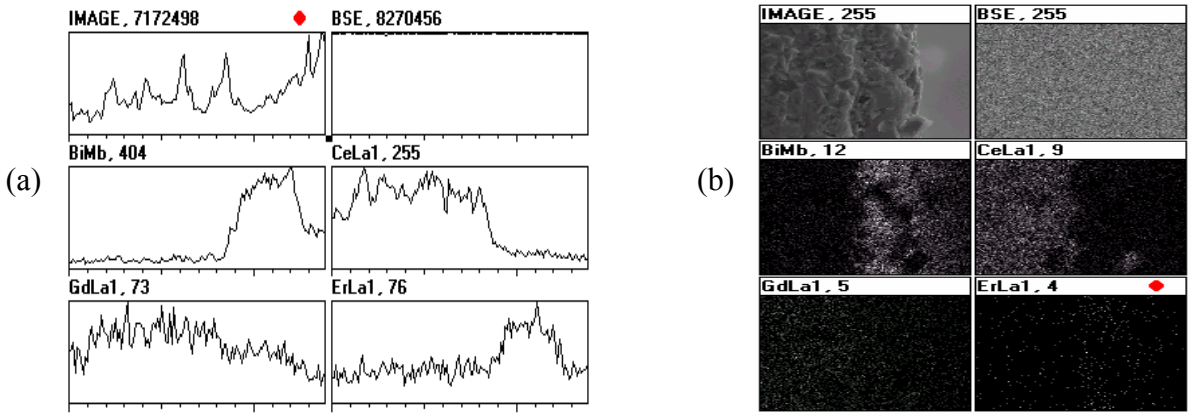

Figure 22. The chemical composition of the bilayer ESB/GDC electrolytes estimated from EDS by X-ray (a) linescan and (b) mapping.

(perhaps by introducing a dispersant). Finally, significant interdiffusion between two phases was not detected from EDS (Fig. 22) of the samples.

3.5 Electrochemical Performance of SDC and Bilayer ESB/SDC Electrolytes

3.5.1 Comparison of Electrochemical Performance of SDC and Bilayer ESB/SDC Electrolytes

Two oxygen concentration cells of the type

$$P_{O_2}, \text{Pt} / (CeO_2)_{0.8}(Sm_2O_3)_{0.1} / \text{Pt}, P_{H_2/H_2O} \quad (1)$$

and

$$P_{O_2}, \text{Au} / (Bi_2O_3)_{0.8}(Er_2O_3)_{0.2}/(CeO_2)_{0.8}(Sm_2O_3)_{0.1} / \text{Pt}, P_{H_2/H_2O} \quad (2)$$

were used to compare the performance of the ESB/SDC bilayer vs. single-layer SDC and to test the effect of thickness ratios of the bilayer electrolyte samples. For the comparison, Au electrodes were deposited onto the ESB layer and Pt paste was coated on the SDC layer of the bilayer ESB/SDC electrolyte for electrodes. Each bilayer was identified as 0.8, 1.3, 9, 25, and 30 ESB/SDC by thickness of ESB layer, see Table 4, which was obtained from profilometry and SEM analysis. Oxygen partial

Table 4. Relative thicknesses of ESB/SDC Electrolytes.

Electrolytes	SDC layer thickness (mm)	ESB film thickness (μm)	Relative thickness
0.8 ESB/SDC	1.601	0.8	5.0×10^{-4}
1.3 ESB/SDC	1.756	1.3	7.4×10^{-4}
10 ESB/SDC	1.499	9	6.0×10^{-3}
25 ESB/SDC	1.5	22	0.015
30 ESB/SDC[W]	1.0	30	0.03

W: relative thickness from previous results (from Wachsman et al. [5])

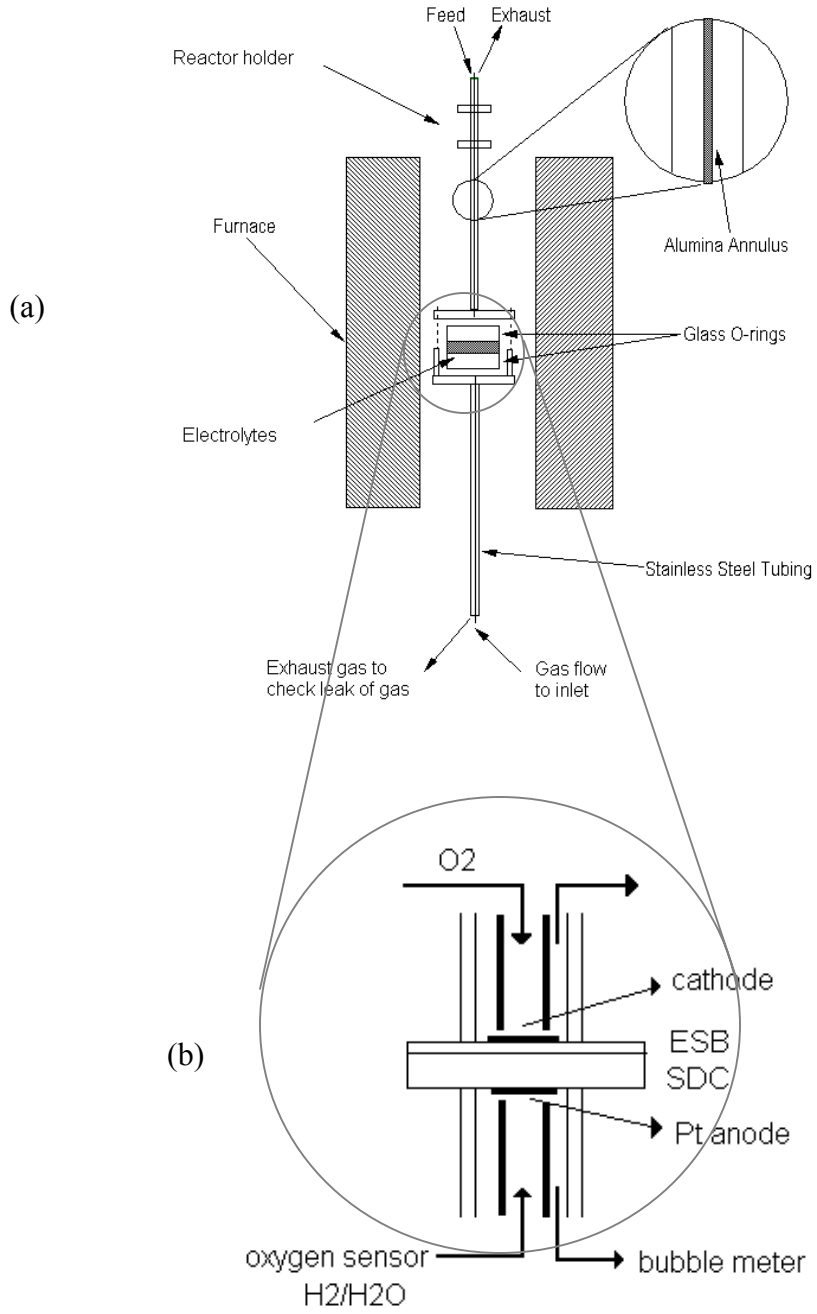

Figure 23. Experimental setup of fuel cell reactor used glass o-rings [26].

pressure (P_{O_2}) was fixed at 0.21 atm. (using air) on the cathode side and all cells were evaluated under identical conditions of H_2/H_2O on the anode side. The OCP of each gas concentration cell was measured over the temperature range 500 °C - 800 °C with a gas flow rate of 60 sccm. The experimental setup is shown in Fig. 23.

In the experimental setup, a vertical *inconel* reactor was used to avoid severe oxidation at high temperature. The reactor consists of two mating flanges with gas tubing welded through the center of

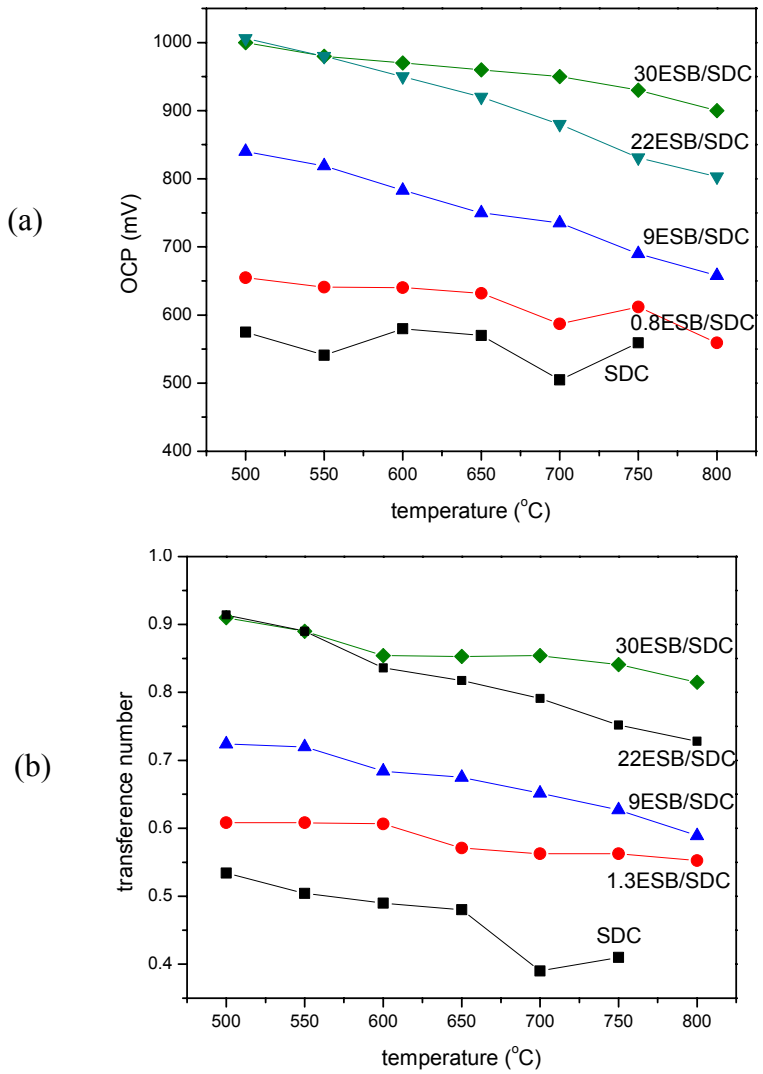

Figure 24. (a) OCP and (b) t_i as a function of temperature for SDC and ESB/SDC electrolytes in the fuel cell mode.

the face to allow for gas flow. The diameter of the gas tubing was 12 mm and the thickness of the ceramic annulus gas tubing to provide electrical insulation between the gold lead wires and the metal gas tube. The flow of gases into the reactor was regulated by calibrated mass flow controllers (Edwards 825, series B). A temperature controller was used in conjunction with a K-type thermocouple to hold the temperature in the reaction zone constant during each test. The oxygen sensor is used to measure the P_{O_2} of the reducing side thereby allowing the calculation of the theoretical (Nernst) OCP and then t_i by comparison with the measured SOFC OCP ($t_i = OCP_{measured}/OCP_{theoretical}$).

Figure 24 shows comparisons of OCP and t_i between a single layer SDC and bilayer ESB/SDC electrolyte as a function of temperature obtained from OCP. measurements, respectively. The ESB/SDC cell showed a substantial increase in OCP and t_i compared to the uncoated SDC cell and the OCP of the

ESB/SDC cell was greater than that of SDC at any temperature. This enhancement in OCP and t_i is due to the ability of the ESB layer to block electronic conduction. The decrease in OCP and t_i with increasing temperature is due to the decreasing ionic domain of the ceria electrolyte.

3.5.2 Effect of the Relative thickness of ESB/SDC electrolytes on OCP and t_{ion}

To investigate the effect of relative thickness of bilayer ESB/SDC electrolytes on OCP and t_i, five cells were prepared by depositing ESB layers via PLD and dip-coating of varying thickness on identical SDC substrates. Because SDC and ESB materials have a high ionic conductivity and relative thickness

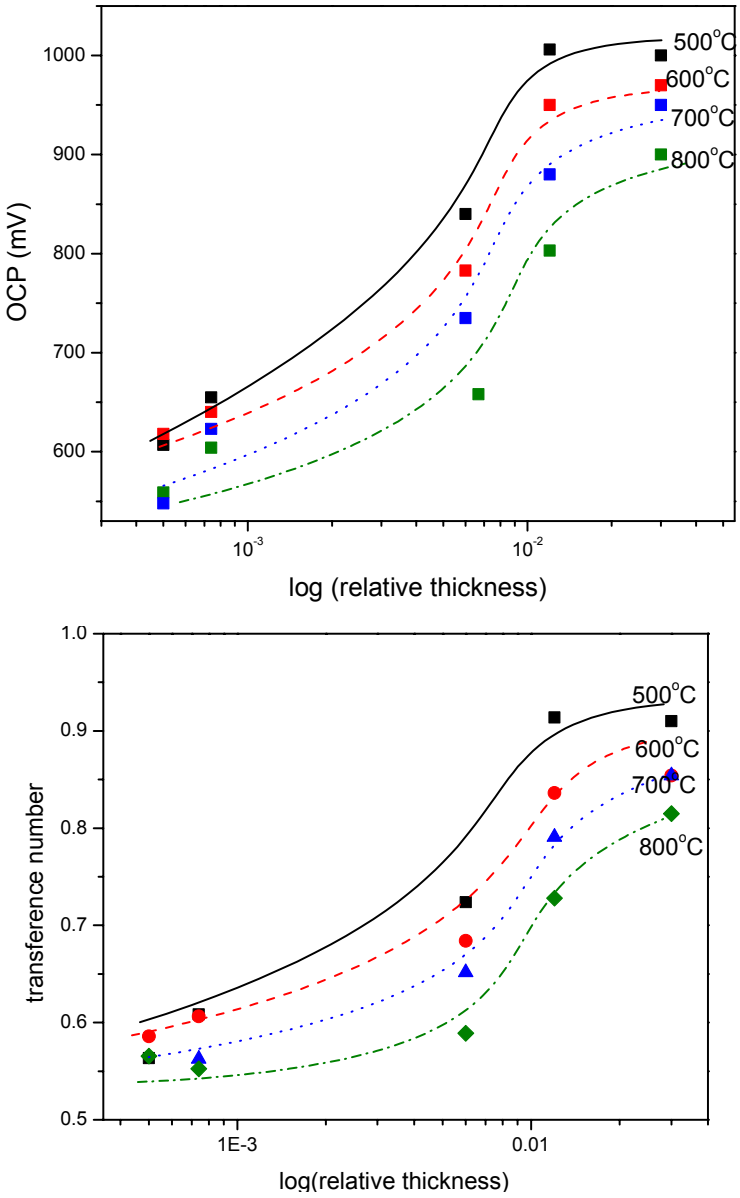

Figure 25. Effect of ESB/SDC relative thickness on (a) OCP and (b) t_i relation of bilayer electrolyte SOFC with air on the cathode side and H_2/H_2O on the anode side

is the important factor, the higher electrochemical performance of cells may be produced by reducing total electrolyte thickness. Table 4 shows the relative thickness of ESB/SDC electrolytes.

Results for the OCP and t_i of ESB/SDC cells as a function of relative thickness are shown in Fig. 25. From 500 °C to 800 °C the OCP and t_i increase considerably with relative thickness of ESB/SDC. Therefore, ESB/SDC cells result in a notable increase in OCP and t_i at all temperatures compared to the single SDC cell. This trend confirms the original postulate outlined in our proposal.

4. CATHODE DEVELOPMENT

In this section we discuss the development of suitable high performance cathodes for bilayered electrolytes. The suitability of the cathodes is dependent on the how little adverse reactions occur between the ESB layer of the bilayer and the cathode. The main parameters determining the performance level of the cathode include its catalytic activity, (electronic and ionic) conductivity and structure/morphology all of which contribute to its polarization.

4.1 Fabrication and Characterization

In order to become familiar with some of the synthesis and characterization techniques and to establish a baseline from which to judge the proposed cathode improvements, dual phase composites of Ag and ESB were examined. Ag powder (0.6-2.0 micron particle size) was purchased from a commercial source. $Er_{0.2}Bi_{0.8}O_{1.5}$ powder was prepared by a conventional ceramic method by combining appropriate amounts of erbium oxide powder and bismuth oxide powder. The combination was ball milled in ethanol using zirconia milling media for 24 hours and dried in air. The resulting powder was then crushed with a mortar and pestle, fine particles were separated through a 325 mesh screen. Calcining was performed at 850 ºC for 10 hours in order to form the appropriate doped-fluorite structure. XRD was performed on this calcined powder to verify that a stable fluorite structure had formed, see Figs. 12, 13 and 15. Ag and ESB powders were combined on a 1:1 volume percent ratio, mixed in a mortar and pestle using, as organic vehicles, polyvinyl butyral (binder, 3 wt.%), dibutyl phthalate (plasticizer), and α-terpinol (solvent). The slurry was mixed to an appropriate viscosity and screen printed onto each side of an ESB electrolyte substrate. The coated samples were fired at 800 ºC. Ag mesh and leads were attached using Ag paste to each electrode.

To test the influence of porosity on electrical performance, 10 vol.% cellulose powder was added to the slurry during the mixing stage. To test the influence of the ionic conducting phase particle size, ESB powders were also prepared by the citrate process using stoichiometric amounts of hydrated nitrate salts $Bi(NO_3)_3$—$X{\cdot}H_20$ and $Er(NO_3)_3$—$5{\cdot}H20$. The reactants were dissolved in de-ionized (DI) water in a Pyrex container. Ethylene glycol and citric acid were added as the solvent and the metal chelating agent, respectively. The solution was slowly heated on a hot plate and carefully monitored until the point where the DI water evaporated. At this point the thermo-chemical reaction between nitrate salts occurred, and a precursor foam was produced. The product was calcined at 700 °C for 2 hrs. The fluorite structure was verified by XRD. SEM revealed that ESB particles prepared by the citrate method

were significantly smaller than those prepared by the conventional solid state ceramic processing method, see Fig. 14. Additional details of both the conventional ceramic and the citrate processes can be found in chapter 3.

To test the effect of cathode thickness, Ag-ESB-no cellulose paste (using ESB prepared by the citrate process) was screen printed to each side of three different ESB pellets using 1 coat on the first pellet, 2 coats on the second pellet, and 4 coats on the third pellet. Electrical characterization of these Ag-ESB composite cathodes was performed by impedance spectroscopy. Impedance measurements were monitored with a Solatron SI 1260 impedance analyzer using frequencies ranging from 0.1 Hz to 10 MHz at temperatures ranging from 400 °C to 700 °C in air (30ccm flow rate).

4.2 Results and Discussion

Plots of cathode resistance as a function of temperature are shown in Figures 26 - 28. Note that in these figures, the subscripts "SST" and "CP" refer to ESB powders prepared by the solid state conventional method and from the citrate process, respectively. As expected, reduced ESB phase particle size led to a reduction in total electrical resistance (Fig. 26). Resistance values were also reduced by an increase in cathode thickness (Fig. 27). One unexpected result was that the cathodes containing 10 % cellulose pore former showed resistance that was an order of magnitude larger than

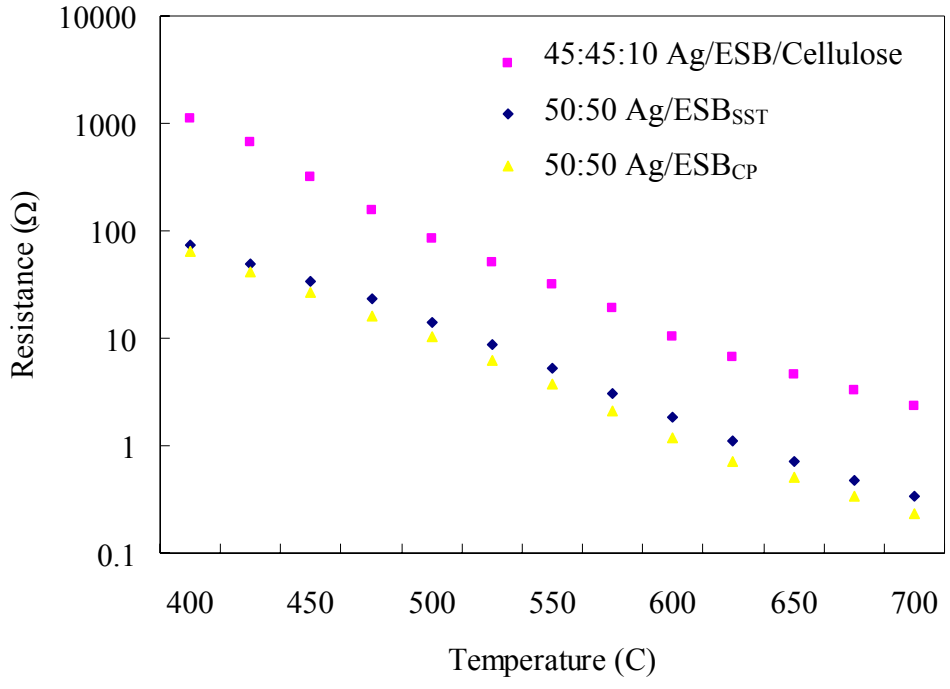

Figure 26. Comparison of electrical resistance as a function of temperature for 45:45:10 Ag/ESB_{CP}/Cellulose, 50:50 Ag/ESB_{SST} and 50:50 Ag/ESB_{CP} cathodes.

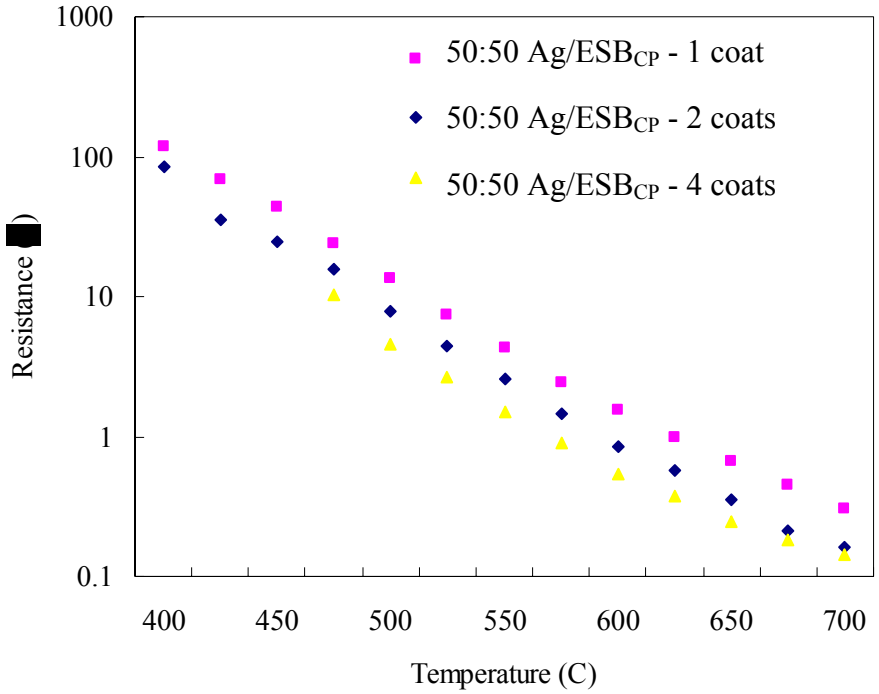

Figure 27. Electrical resistance as a function of temperature and coating layers for 50:50 Ag/ESB_{CP} cathodes.

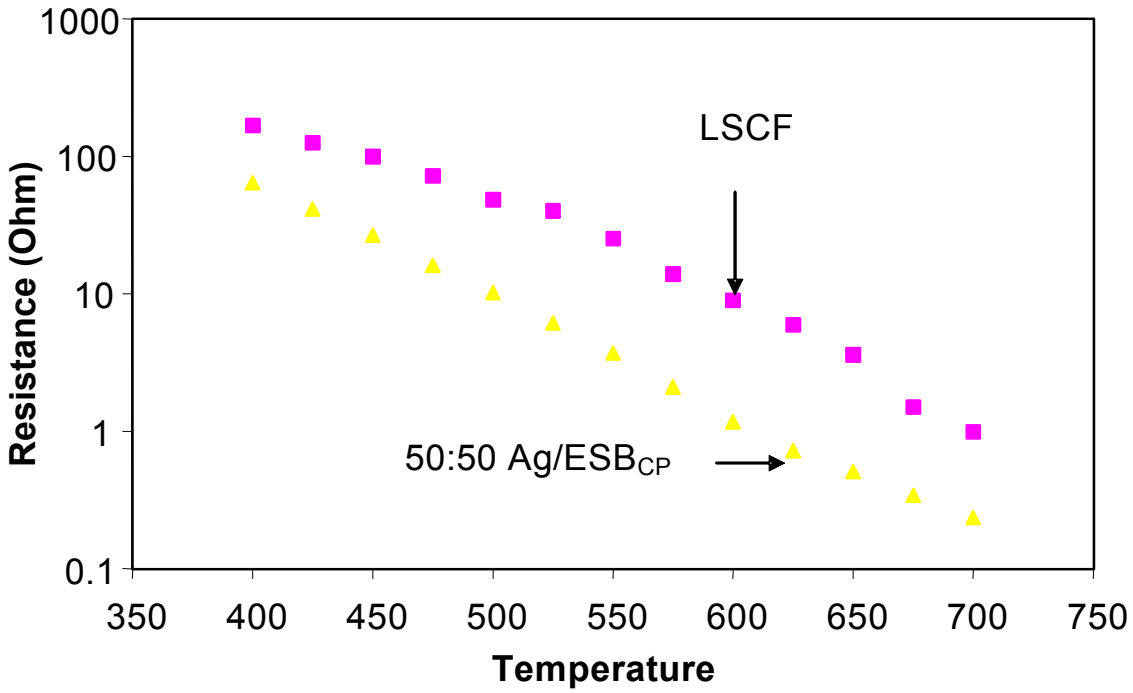

Figure 28. Comparison of electrical resistance as a function of temperature for 50:50 Ag/ESB_{CP} and LSCF cathodes.

those containing no pore former, Fig. 26. This result could be attributed to the inherent porosity of the Ag-ESB-no cellulose cathode slurry. The additional 10 vol.% of porosity could reduce the connectivity of both Ag and ESB phases, resulting in the poor performance observed for thin cathodes. The porosities of these cathodes will be examined by SEM in the near future to verify this point. Obviously we have not reached the optimum thickness for the cathodes as Fig. 27 indicates that better performance should be attained with a thicker cathode.

Finally, the LSCF cathode didn't perform as well as the Ag-ESB cathodes, however, its porosity has not been optimized as yet and we anticipate improved performance from both, as more work is done in this area. Figure 28 shows that the LSCF cathode is consistently outperformed by the Ag/ESB_{CP} cathode.

5. MODELING THE THERMO-MECHANICAL PROPERTIES OF MIECS

In this section, we extend the electrochemical model developed earlier, for the spatial distribution and transport of defects in an MIEC [6, 7], to the thermo-mechanical properties of MIECs. This is made possible by application of rudimentary expressions for the bond energy, E_{bond}, elastic modulus, Y, and fracture toughness, K_{IC}, of a ceramic [28]. More sophisticated expressions for these properties can be used, however, if testing with experimental data reveals it is necessary.

The maximum bond energy (i.e., just before cleavage) between atoms in a ceramic may be approximated by [28]

$$E_{bond} = \left(1 - \frac{m}{n}\right)\frac{B}{a^m} \tag{5.1}$$

where a is the lattice constant; B, n and m are empirically determined constants (typically $m < n$) and a is the lattice constant. In the literature [29, 30] a has been shown to increase linearly with the oxygen vacancy concentration, c_V. Thus, the elastic modulus, Y, may be approximated as follows

$$Y(x) \approx \frac{B'}{a^{m+3}} = \left(b_1 c_V(x) + B' a^\circ\right)^{-(m+3)} \tag{5.2a}$$

or

$$Y(x)/Y^\circ \approx \left(\sqrt[m+3]{Y^\circ}\, b_1 c_V(x) + 1\right)^{-(m+3)} \tag{5.2b}$$

In addition, fracture toughness, K_{IC} , is related to the elastic modulus as follows

$$K_{I_C} = \sqrt{2 E_{surf} Y} \tag{5.3}$$

where, E_{surf} is the intrinsic surface energy per unit area and [28]

$$E_{surf} \propto a^{-3} \tag{5.4}$$

Therefore, by combining Eqs. (5.2) and 5.3 may be approximated as

$$K_{IC}(x) \approx \sqrt{2\left(B'' a^{-3}\right) Y} = \left(b_2 c_V(x) + 2B' B'' a^\circ\right)^{-\frac{m+6}{2}} \tag{5.5a}$$

or

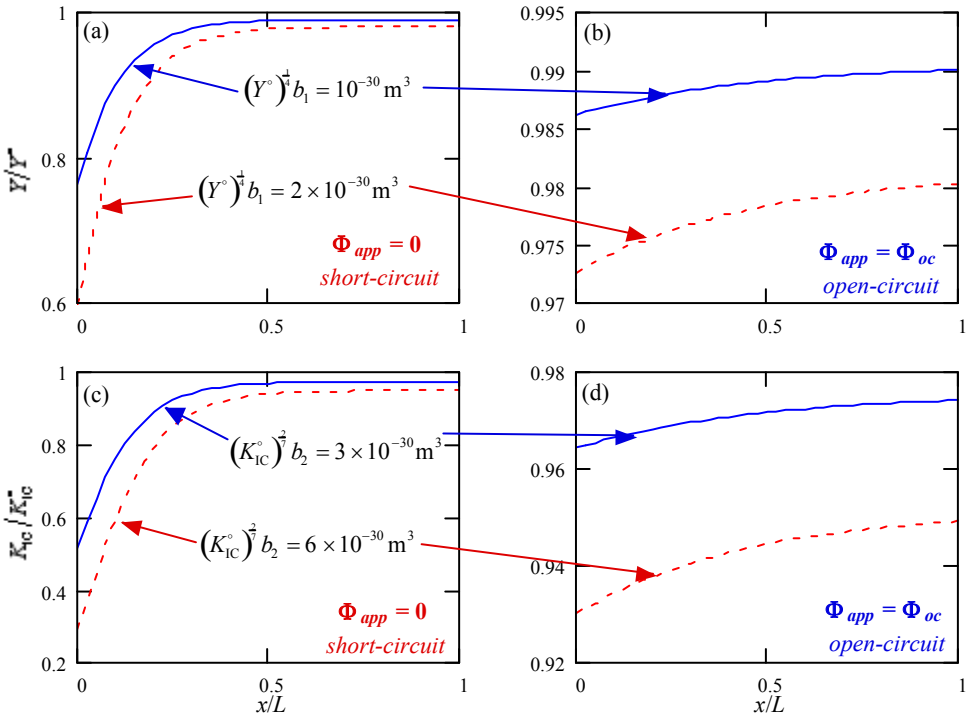

Figure 29. Normalized profiles of (a) Y(*short-circuit*) (b) Y(*open-circuit*) (c) K_{IC}(*short-circuit*) and (d) K_{IC}(*open-circuit*).

$$K_{IC}(x)/K_{IC}^\circ \approx \left(\sqrt[m+6]{\left(K_{IC}^\circ\right)^2} b_2 c_V(x) + 1 \right)^{-\frac{m+6}{2}} \tag{5.5b}$$

where, B', B'', b_1 and b_2 are empirically determined constants (related to B, n, and m) and the superscript "°" refers to when the MIEC is stoichiometric—i.e., $c_V(x) = 0$ (no dopant) or $c_V(x) = c_A/2$, where c_A is the dopant concentration.

$Y(x)$ and $K_{IC}(x)$ are plotted in Fig. 29 for $m = 1$ (typical value for m if the attractive forces between ions in the lattice are mainly Coulombic) and for two different values of the constants $(Y^\circ)^{\frac{1}{4}} b_1$ and $(K_{IC}^\circ)^{\frac{2}{7}} b_2$, as indicated in the figure. Fig. 30 shows that, depending on the material constants, mechanical properties can vary significantly over the thickness of the electrolyte. Moreover, the degree of variation is a function of the SOFC operating conditions. As one may expect, Y and K_{IC} both decrease as the reducing/fuel side of the electrolyte is approached (at $x = 0$) and c_V increases.

However, the most crucial result shown in Fig. 29 is the rapid degradation of the mechanical properties towards the anode side of the electrolyte when (the maximum) current passes through the cell. This shows that the probability of fracture increases with current density. Also, these results imply that fracture is likely to initiate on the anode side of the SOFC. Clearly, the electrochemical model developed above, enables the determination of the thermo-mechanical properties of SOFCs.

REFERENCES

1. K. Mehta, S. J. Hong, J. -F. Jue and A. V. Virkar, in *Solid Oxide Fuel Cells III*, S. C. Singhal and H. Iwahara, ed., PV 93-4, p. 92, Electrochem. Soc. Proc. Series.

2. P. Soral, U. Pal and W. Worrell, *J. Electrochem. Soc.* **145** (1998) 99.

3. P. Shuk, H. -D. Wiemhöfer, U. Guth, W. Gopel and M. Greenblatt, *Solid State Ionics* **89** (1996) 179.

4. A. M. Azad, S. Larose and S. A. Akbar, *J. Mat. Sci*. **29** (1994) 4135.

5. E.D.Wachsman, P. Jayaweera, N. Jiang, D.M. Lowe, B.G. Pound, *Journal of the Electrochemical Society*,**144** (1997) 233.

6. K. Duncan, Ph. D. Thesis, University of Florida (2001).

7. E. D. Wachman and K. L. Duncan, Stable High Conductivity Bilayered Electrolytes for Low Temperature Solid Oxide Fuel Cells, DOE Annual Report Contract No. DE-AC26-99FT40712, 2002.

8. S. Ohara, R. Maric, X. Zhang, K. Mukai, T. Fukui, H. Yoshida, T. Inagaki, K. Miura, *Journal of Power Sources*, **86** (2000) 455.

9. J. Will, A. Mitterdorfer, C. Kleinlogel, D. Perednis, L.J. Gaukler, *Solid State Ionics*, **131** (2000) 79.

10. S. deSouza, S.J. Visco, L.C. DeJonghe, *Journal of the Electrochemical Society*, **144** (1997) L35.

11. L. W. Tai, M. M. Nasrallah, H. U. Anderson, in : S. C. Singhal, H. Iwahara (Eds.), *Proc. 3rd Int. Symp. Solid Oxide Fuel Cells, The Electrochemical Society Proceeding Series* (1999) p. 241, Pennington, NJ.

12. L. W. Tai, M. M. Nasrallah, H. U. Anderson, M. A. Alim, *Journal of the Electrochemical Society*, **142** (1995) 491.

13. L. W. Tai, M. M. Nasrallah, H. U. Anderson, D. M. Sparlin, S. R. Sehlin, *Solid State Ionics*, **76** (1995) 273.

14. K. Zheng, B.C.H. Steele, M. Sahibzada, I.S. Metcalfe, *Solid State Ionics*, **86-88** (1996)1241.

15. W. Huang, P. shuk, and M. Greenblatt, *Solid State Ionics*, **100** (1997) 23.

16. I. Y. Yoon, H. S. Yoon, and B. H. Kim, *J. KIEEME* 11 **1** (1998) 18.

17. H. S. Yoon, S. W. Choi, D. Lee, and B. H. Kim, *J. Power Sources* **93** (2001) 1.

18. H. Arai, in *Proceedings of the International Syposium on Solid Oxide Fuel Cells*, November 13-14, 1989, Nagoya, Japan, eds. O. Yamamoto, M. Dokiya, and H. Tagawa, Science House, Tokyo, Japan (1989) 12.

19. K. Tsukamoto, F. Uchiyama, Y. Kaga, Y. Ohno, T. Yanagisawa, A. Monma, Y. Takahagi, M. J. Lain, and T. Nakajima, *Solid State Ionics*, 40-41 (1990) 1003.

20. T. Setoguchi, M. Sawano, E. Eguchi, and H. Arai, *Solid State Ionics*, **40-41** (1990) 502.

21. H. Arai, in *Proceedings of the International Syposium on Solid Oxide Fuel Cells*, November 13-14, 1989, Nagoya, Japan, eds. O. Yamamoto, M. Dokiya, and H. Tagawa, Science House, Tokyo, Japan (1989) 58.

22. M. F. Carolan and J. N. Michaels, *Solid State Ionics*, **25** (1987) 207

23. N. Nicoloso, B. Leibold, and H. U. Habermeier, in Laser Ablation of Electronic Materials, eds. E. Fogarassy and S. Lazare, Elsevier, Amsterdam, The Netherlands (1992) 385

24. S. Souza, S. J. Visco, and L. C. De Jonghe, *J. Electrochem. Soc*., **144** (1997) L35

25. J. Will, A. Mitterdorfer, C. Kleinlogel, D. Perednis, and L. J. Gauckler, *Solid State Ionics*, **131** (2000) 79

26. T. L. Clites, M.D. Thesis, *Development of Stable Mixed-Conducting Bilayer Perovskite Membranes for the Direct Conversion of Methane to Syngas*, University of Florida, 1999

27. R. Doshi, V. L. Richards, J. D. Carter, X. Wang, and M. Krumpelt, *J. Electrochem. Soc*. **146** (1999) 1273

28. M. Barsoum, in Fundamentals of Ceramics (McGraw-Hill, 1977).

29. D-J. Kim, *J. Amer. Ceram. Soc.* **72** (1989) 1415.

30. M. O. Zacatea, L. Minervinia, D. J. Bradfielda, R. W. Grimes and K. E. Sickafus *Solid State Ionics* **128**, (2000) 243.